Hydroxyl Groups on Cellulose Nanocrystal Surfaces form Nucleation Points for Silver Nanoparticles of Varying Shapes and Sizes

Dafne Musino, Camille Rivard, Gautier Landrot, Bruno Novales, Thierry Rabilloud, Isabelle Capron

Journal Pre-proofs

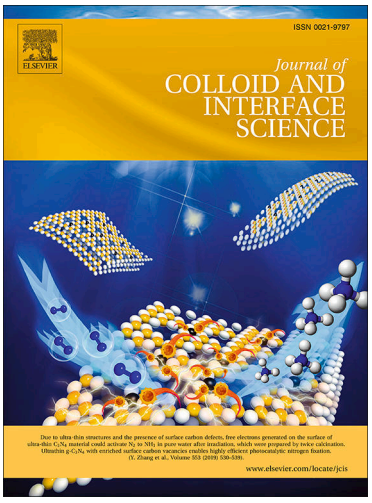

Regular Article

Hydroxyl Groups on Cellulose Nanocrystal Surfaces form Nucleation Points for Silver Nanoparticles of Varying Shapes and Sizes

Dafne Musino, Camille Rivard, Gautier Landrot, Bruno Novales, Thierry Rabilloud, Isabelle Capron

PII: S0021-9797(20)31271-6
DOI: https://doi.org/10.1016/j.jcis.2020.09.082
Reference: YJCIS 26987

To appear in: *Journal of Colloid and Interface Science*

Received Date: 20 July 2020
Revised Date: 15 September 2020
Accepted Date: 21 September 2020

Please cite this article as: D. Musino, C. Rivard, G. Landrot, B. Novales, T. Rabilloud, I. Capron, Hydroxyl Groups on Cellulose Nanocrystal Surfaces form Nucleation Points for Silver Nanoparticles of Varying Shapes and Sizes, *Journal of Colloid and Interface Science* (2020), doi: https://doi.org/10.1016/j.jcis.2020.09.082

Graphical abstract

Hydroxyl Groups on Cellulose Nanocrystal Surfaces form Nucleation Points for Silver Nanoparticles of Varying Shapes and Sizes

*Dafne Musino,[a] Camille Rivard, [b,c] Gautier Landrot,[b] Bruno Novales,[a] Thierry Rabilloud [d] and Isabelle Capron[a]**

[a] INRAE, BIA, 44316 Nantes, France

[b] SOLEIL Synchrotron, L'Orme des Merisiers, Gif-sur-Yvette, 91192 Saint-Aubin, France

[c] INRAE, TRANSFORM, 44316 Nantes, France

[d] Univ. Grenoble Alpes, CNRS, CEA, IRIG, SYMMES, Laboratoire de Chimie et Biologie des Métaux, 38000 Grenoble, France

* *Author for correspondence: isabelle.capron@inrae.fr,* INRAE, BIA, Rue de la Geraudiere, 44316 Nantes, France. Tel : +33 2 40 67 50 43

dafne.musino@inrae.fr

camille.rivard@synchrotron-soleil.fr

gautier.landrot@synchrotron-soleil.fr

bruno.novales@inrae.fr

thierry.rabilloud@cnrs.fr

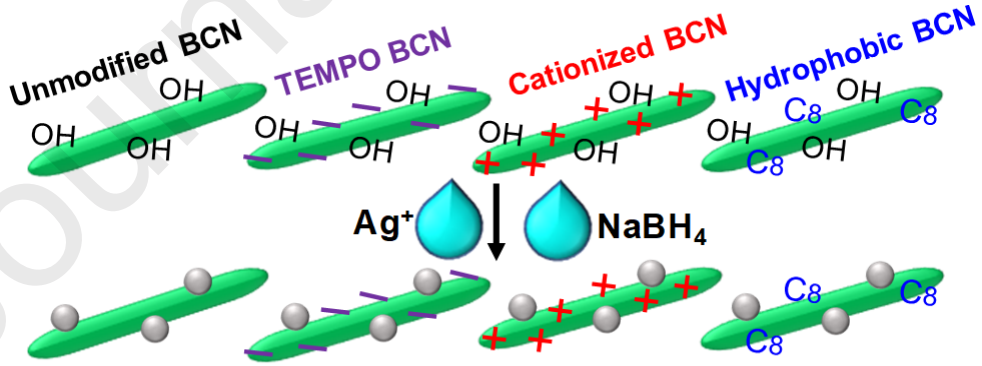

Hydroxyl Groups on Cellulose Nanocrystal Surfaces form Nucleation Points for Silver Nanoparticles of Varying Shapes and Sizes

*Dafne Musino,[a] Camille Rivard, [b,c] Gautier Landrot,[b] Bruno Novales,[a] Thierry Rabilloud [d] and Isabelle Capron[a]**

[a] INRAE, BIA, 44316 Nantes, France

[b] SOLEIL Synchrotron, L'Orme des Merisiers, Gif-sur-Yvette, 91192 Saint-Aubin, France

[c] INRAE, TRANSFORM, 44316 Nantes, France

[d] Univ. Grenoble Alpes, CNRS, CEA, IRIG, SYMMES, Laboratoire de Chimie et Biologie des Métaux, 38000 Grenoble, France

**Author for correspondence: isabelle.capron@inrae.fr,* INRAE, BIA, Rue de la Geraudiere, 44316 Nantes, France. Tel : +33 2 40 67 50 43

dafne.musino@inrae.fr

camille.rivard@synchrotron-soleil.fr

gautier.landrot@synchrotron-soleil.fr

bruno.novales@inrae.fr

thierry.rabilloud@cnrs.fr

Abstract. In this study, we investigate the interactions between the cellulose surface and Ag nanoparticles (AgNPs) for the purpose of manufacturing hybrid nanomaterials using bacterial cellulose nanocrystals (BCNs) as a model substrate. We focus on the role of the BCN surface chemistry on the AgNP nucleation obtained by chemical reduction of Ag^+ ions. Homogeneous hybrid suspensions of BCN/AgNP are produced, regardless of whether the BCNs are quasi-neutral, negatively (TBCNs) or positively charged (ABCNs). The characterization of BCN/AgNP hybrids identifies the –OH surface groups as nucleation points for AgNPs, of about 20 nm revealing that surface charges only improve the accessibility to OH groups. X-ray Absorption technics (XANES and EXAFS) revealed a high metallic Ag_0 content ranging from 88% to 97%. Moreover, the grafting of hydrophobic molecules on a BCN surface (HBCNs) does not prevent AgNP nucleation, illustrating the versatility of our method and the possibility to obtain bifunctional NPs. A H_2O_2 redox post-treatment on the hybrid induces an increase in AgNPs size, up to 90 nm as well as a shape variation (i.e., triangular). In contrast, H_2O_2 induces no size/shape variation for aggregated hybrids, emphasizing that the accessibility to –OH groups ensures the nucleation of bigger Ag nano-objects.

Keywords. Bacterial cellulose nanocrystal (BCN), hydroxyl groups, surface modification, silver nanoparticles (AgNPs), AgNP size-shape variation, hydrophobic BCN, hybrid nanomaterial.

1. Introduction

Cellulose is an almost inexhaustible biopolymer extracted from wood, cotton, algae, tunicates or bacteria [1–3], leading to variation in dimensions and structural organization [4]. Cellulose displays interesting properties such as high water retention capacity, high wet strength, low density, bio-compatibility, non-toxicity and biodegradability, which make it very appropriate for several applications in biomedicine and pharmacology [5–7], cosmetics [8], paper and textiles [9]. Cellulose can also be hydrolyzed to increase its crystallinity, commonly by acid hydrolysis, leading to the so-called cellulose nanocrystals (CNCs) [10]. While the extraction of plant-sourced cellulose often requires the use of hazardous chemicals, bacterial cellulose (BC) is mainly secreted extracellularly by certain bacteria such as *Gluconacetobacter xylinu* [1]. Therefore, bacterial cellulose nanocrystal (BCN) contain no functional groups other than hydroxyl groups [11] and thanks to its high chemical purity, they are particularly interesting for food and medical applications.

To confer antimicrobial properties to CNCs, as to BCNs, it is quite common to graft or nucleate metallic nanoparticles (e.g., Cu, Ag, ZnO, Au) on their surface [12–15]. Among others, silver nanoparticles (AgNPs) have been widely studied. A silver precursor is generally incorporated by addition of a salt such as silver nitrate ($AgNO_3$), and several experimental methods (e.g., UV radiation [16,17], hydrazine reduction [18]) have been proposed to nucleate AgNPs on the cellulose nanocrystal surface, thus obtaining a hybrid material (i.e., CNC/AgNPs). Chemical reduction is one of the most common ways to synthesize metallic NPs, and sodium borohydride ($NaBH_4$) [19–22] is reported to be one of the most efficient reducing agents, inducing the rapid formation of 2-3-nm AgNPs [23]. NH_4OH [24] and ascorbic acid [25] can also be used to reduce Ag^+ ions into AgNPs. To carry out this chemical AgNP synthesis, capping agents or stabilizers (e.g., trisodium citrate: TSC; polyvinylpirrolidine: PVP; Cetrimonium bromide: CTAB) are often introduced to better control the morphological properties of AgNPs, preventing their aggregation [26–28]. In other cases, nanocellulose is proposed as both a support and a reducer for the generation of metallic nanoparticles [29]. Xiong et al. [30] claim that cellulose promotes the generation of AgNPs and dendritic Ag nanostructures thanks to the extensive presence of surface hydroxyl groups. Furthermore, various surface modifications of CNCs can be performed (e.g., amidation, oxidation, esterification, etherification) [10], possibly affecting the reduction of AgNPs on the CNC surface. Most of the studies concerning CNC/AgNP hybrids [31–33] indicate how the introduction of negative surface charges (i.e., via TEMPO-mediated oxidation [32]) can provide the high-binding capability for the transition of metal species such as Ag^+ ions. Moreover, other surface modifications can be performed on the CNC surface to extend the possible application fields. For example, cationized cellulose can be produced by grafting different molecules on the cellulose surface (e.g., HPTMAC: hydroxypropyltrimethylammonium chloride [34], BriBBr: a-bromoisobutyryl bromide [35], HDTMA: hexadecyltrimethylammonium [36] or pyridinium [37]) so that it can be used for papermaking, cosmetics and drug-delivery [38]. The work of Shateri Khalil-Abad et al. [39] reveals that surface-

modification of cellulose cotton fibers by 3-chloro-2-hydroxypropyl trimethyl ammonium chloride (CHPTAC) affects the absorption of AgNPs on the fiber surface. Indeed, such an adsorption is greater on cationized cellulose fibers than on untreated ones. To obtain these cationized fibers, Dong et al. [40] propose to graft ammonium ions onto the surface, thus creating two different pathways for the deposition of metal NPs (e.g., Au, Pt, Pd): the first one based on the electrostatic assembly of metal nanoparticles capped with negative citrate ions, and a second one where negative metal complex ions are adsorbed onto the cationic substrate and then reduced. Both approaches lead to a high surface coverage of the CNC surface by metallic nanoparticles.

CNCs can also be made hydrophobic to allow their dispersion in non-aqueous solvents. To do this, one of the most widely used approaches is amidation, where coupling agents are grafted onto TEMPO-oxidized nanocrystals [10]. Araki et al. [41] propose the grafting of poly(ethylene glycol) with a terminal amino group onto the surface of TEMPO-oxidized CNCs. Zhang et al. [42] use a similar experimental approach to covalently functionalize CNCs via peptide coupling chemistry with different alkylamines (e.g., propylamine, n-butylamine, amylamine, hexylamine, heptylamine). Hu et al. [43] propose using tannic acid to covalently attach primary amine with a long alkyl chain (i.e., decylamine) to the CNC surface. In addition, Cunha et al. [44] produced inverse emulsions, tailoring the hydrophobicity of CNCs and nanofibrillated cellulose by chemical modification with lauroyl chloride (C_{12}). However, no studies have proposed bifunctional hybrids, using hydrophobically-modified CNCs as substrates for AgNP nucleation.

As for nanocellulose surface modification, AgNP characteristics (e.g., size, shape, crystalline structure) can strongly influence the final properties of the CNC/AgNP hybrid system. Some works report simple techniques for a shape- and size-selective synthesis of Ag nanostructures (e.g., from spherical AgNPs to triangular-shaped AgNPs or Ag nanoprisms, denoted AgNPrisms [45]) based on the use of hydrogen peroxide (H_2O_2) redox post-treatment [20,21,46,47], as well as photo-induced [48] or solution-phase [49] methods. In particular, the size-shape transformation of AgNPs achieved with H_2O_2 relies to redox capabilities linked to the autocatalytic decomposition on the Ag surface. These AgNPrisms are anisotropic (i.e., their lateral dimension is greater than their thickness) and are thus characterized by a strong localized surface plasmon resonance (LSPR). Their resulting size- and shape-dependent optical properties make them suitable for sensors [50,51] and biological imaging [52], catalysts [53], nanophotonic devices and circuits [54,55]. Parnklang et al. [46] show the shape transformation from spherical AgNPs to AgNPrisms when H_2O_2 oxidizes the AgNPs to Ag^+ ions and thus reduces them into Ag atoms in nanometric silver particles. The H_2O_2 redox post-treatment has also been applied to hybrid systems. Jiang et al. [20] propose the fabrication of films made of AgNPrisms and TEMPO-oxidized cellulose nanofibrils, which work as capping and shape-regulating agents. The presence of a predominant (111) peak in the XRD pattern allows them to affirm that AgNPrisms are bounded to cellulose nanofibers.

The result is that hybrids made of AgNPs fixed on the CNC surface have been produced, whereas the interactions and binding mechanisms have not been studied in detail [29,31,56]. In this paper, we propose to perform different surface modifications on BCNs in order to shed light on the effective role of cellulose nanocrystal surface chemistry on the nucleation of AgNPs. We also prepared bifunctional NPs that combine a hydrophobic surface and AgNPs. Moreover, we investigated the impact of the CNC surface modification on the H_2O_2 redox post-treatment, linking the size and shape variation of AgNPs to their physicochemical characteristics (i.e., AgNP structure and oxidation state).

2. Materials and Methods

Chemicals. Food grade nata de coco was purchased from AROY-D (Thailand). All the other products were purchased from Sigma-Aldrich (France) and used as received without further purification: silver nitrate ($AgNO_3 \geq 99\%$), sodium borohydride ($NaBH_4 \geq 96\%$), 2,2,6,6-Tetramethylpiperidine 1-oxyl (TEMPO: 98.8%), sodium bromide (NaBr: 99%), sodium hypochlorite solution (NaClO: 10% RT), cholaminchloride hydrochloride (AETMA: 99%; pKa = 7), octylamine (C_8: 99%; pKa = 10), N-hydroxysuccinimide (NHS), N-(3-dimethylaminopropyl)-N′-ethylcarbodiimide (EDC), hydrogen peroxide 30% (H_2O_2). For all the aqueous suspensions, ultra-pure water was used.

Synthesis of uncharged BCNs. For the preparation of BCNs, the experimental procedure proposed by Kalashnikova et al. [57] was followed. Briefly, nata de coco cubes were dialyzed in ultra-pure water for 9 days, after which they were ground in a Waring blender, suspended in 0.5 N NaOH solution, and stirred for 2 h at 70°C. Finally, the sample was rinsed using ultra-pure water. A whitening treatment was performed twice, dispersing the slurry in a $NaClO_2$ solution (8.5 g/L) in a sodium acetate buffer (pH = 4.5) and stirring it for 2 h at 70°C. The bleached cellulose was rinsed with distilled water and then hydrolyzed with 2.5 M HCl solution at 70°C for 2 h. The suspension was centrifuged three times (10 min., 10000 g) and dispersed in ultra-pure water up to pH > 5. The final BCN suspension was again dialyzed against ultra-pure water for one week and finally homogenized by ultrasound (amplitude = 20; 5 min). The BCN content in the suspension (around 2 g/L) was determined by a drying test.

Synthesis of anionic BCNs mediated via TEMPO oxidation (TBCNs). The experimental protocol for the BCN surface carboxylation via TEMPO-mediated oxidation was adapted from the method proposed by Araki et al. [58]. A quantity of 100 mL of BCN suspension (2 g/L) was mixed with 0.25 g of NaBr and 0.05 g of TEMPO, after which 2.5 mL of NaClO were added to start the BCN carboxylation, leading to a pH increase. The resulting suspension was stirred for 24 h at room temperature while maintaining the pH at 10.3 through the controlled addition of 0.1 M NaOH solution using an automatic titrator (Metrohm 901 Titrando, France). The final suspension was centrifuged twice (10 min; 10000 g), dispersed in ultra-pure water while maintaining the BCN concentration at 2 g/L and, finally, homogenized by ultrasound (amplitude = 10; 5 min). The sample was dialyzed

against ultra-pure water for one week to remove any residual contaminants (dialysis bath volume to sample volume = 10:1).

Synthesis of cationic BCNs (ABCNs). For the BCN surface modification by AETMA, the coupling method proposed by Zhang et al. [42] was used with several modifications, working in a H_2O medium instead of N,N-dimetilformammide (DMF). A quantity of 100 mL of TBCN suspension (2 g/L) was mixed for 5 min at room temperature with 230 mg of EDC. Then, 180 mg of NHS were added and the suspension was stirred for a further 30 min. Finally, a quantity of 210 mg of AETMA were introduced and the sample was stirred for 24 h at room temperature while maintaining the pH at 7 through the controlled addition of 0.1 M NaOH solution using an automatic titrator (Metrohm 901 Titrando, France). The final suspension was centrifuged to remove unreacted residual molecules and dispersed in ultra-pure water to be homogenized by ultra-sound (amplitude = 10; 5 min). The suspension was dialyzed for one day against a KNO_3-saturated solution to promote ion exchange from chloride to nitrate, and then against ultra-pure water for one week (dialysis bath volume to sample volume = 10:1).

Synthesis of hydrophobic BCNs (HBCNs). To obtain HBCNs, the TBCNs were functionalized with alkyl chains (C_8) using a coupling method similar to the one previously proposed for the preparation of the ABCNs in suspension. A quantity of 60 mL of TBCN suspension (2 g/L) was stirred for 5 min at room temperature with 230 mg of EDC and for an additional 30 min after the addition of 180 mg of NHS. In another beaker, a volume of 270 µL of octylamine (C_8) were dissolved in 40 mL of absolute ethanol and added drop-by-drop to the TBCN suspension. The sample was stirred for 24 h at room temperature while maintaining the pH at 10 by the addition of 0.1 M NaOH solution controlled by an automatic titrator (Metrohm 901 Titrando, France). The suspension was then dialyzed against a 60/40 %v/v water/ethanol mixture for 3 days to remove the unreacted residual molecules. The final HBCN concentration was found to be around 2 g/L.

A schematic representation of the various BCN surface modifications and the corresponding scanning transmission electron microscopy (STEM) images are reported in Fig. 1.

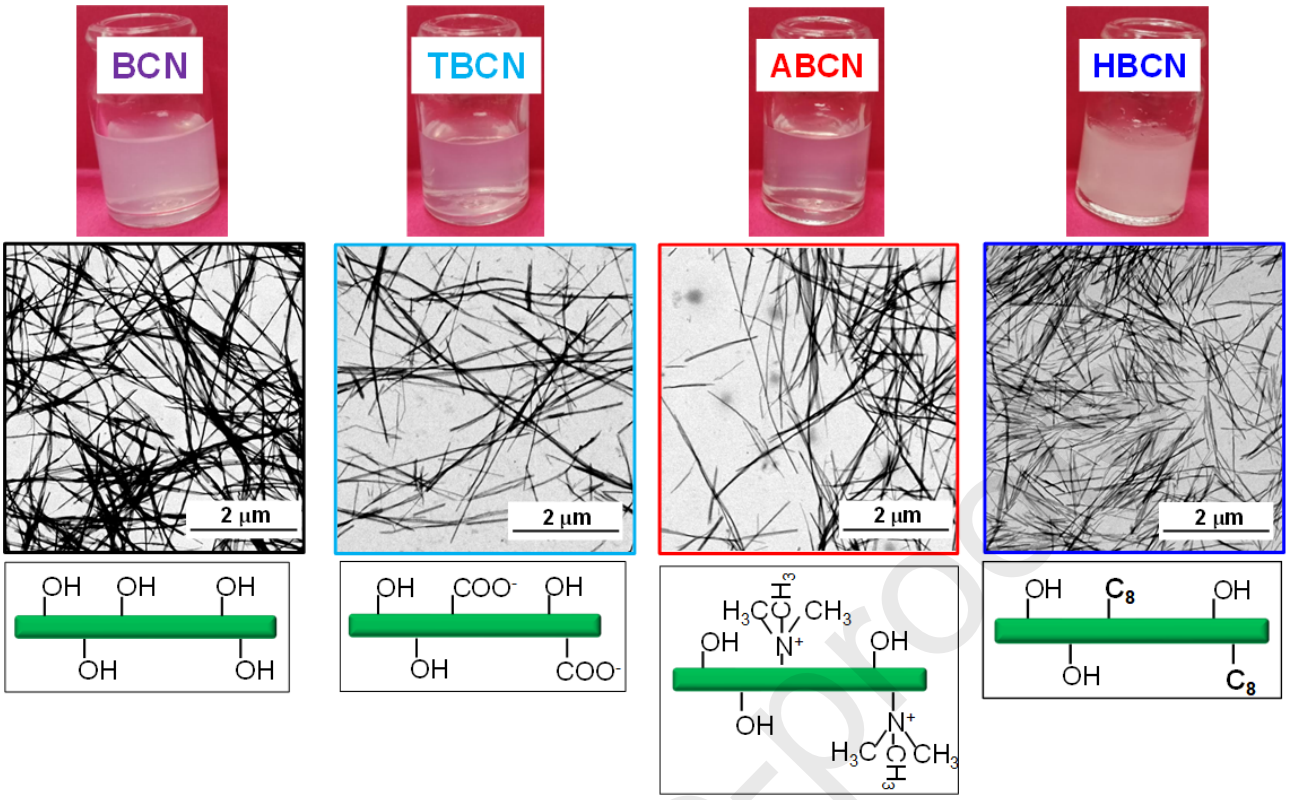

Fig. 1. BCN, TBCN, ABCN and HBCN suspensions: visual appearance (top line), STEM images (middle line) and scheme of various surface modifications (bottom line).

Synthesis of BCN/AgNP hybrids. Both $AgNO_3$ and $NaBH_4$ solutions were freshly prepared just before the experimental session, and the $NaBH_4$ aqueous solution was placed in ice to minimize its decomposition. $AgNO_3$ aqueous solution (300 µL, 50 mM) was added to 10 mL of BCN water suspension and mixed for 1 min at room temperature. The $NaBH_4$ aqueous solution (500 µL, 100 mM) was then introduced to reduce Ag^+ ions to AgNPs, immediately turning the suspension from translucent to light-yellow. The final hybrid suspension was stirred at room temperature for 24 h, protected by light using aluminum foil to prevent silver oxidation, and then dialyzed against water for 24 h. The procedure produced hybrid suspensions with BCNs, independently of prior surface modifications of the BCN.

H_2O_2 redox post-treatment. The modification of AgNP characteristics was performed by adding H_2O_2 to the BCN/AgNP initial hybrid suspension. From now on, the AgNPs obtained after the addition of H_2O_2 will be generically indicated as AgNPs_H_2O_2 and, more specifically, as AgNPrisms when they reach a triangular shape. Immediately after the reduction by $NaBH_4$, various amounts of H_2O_2 (i.e., 0, 40, 80, 120, 160, 250 µL) were added to obtain various H_2O_2/AgNP mass ratios, α (i.e., 0, 0.08, 0.17, 0.25, 0.33, 0.52). The H_2O_2 introduction induces an exothermic reaction associated with the gas bubbles formation associated to the H_2O_2 decomposition [21]. The color of the sample gradually varied from yellow to blue with the introduction of H_2O_2. The final hybrid was dialyzed against ultra-pure water for 24 h.

Characterization. For FTIR measurements, the pure and surface-modified BCN suspensions were freeze-dried using a LYO GT2 lyophilizer (SRK System Technik, Germany; T = - 90°C; 1.5 10^{-2} mbar). A quantity of 2 mg of freeze-dried sample was homogenized with 120 mg of KBr and the resulting powder was compressed (5 tons; 5 s) to obtain a circular pellet. The FTIR analysis were performed using a Nicolet iS50 FTIR spectrometer (Thermo Fisher Scientific, USA) and the spectra were determined to be in the 400 – 4000 cm^{-1} range, with a resolution of 4 cm^{-1}. Each spectrum was the average of 200 scans collected in absorbance mode and examined using OMNIC™ software (Thermo Fisher Scientific, USA).

The conductivity of BCN, TBCN, ABCN and HBCN aqueous suspensions was automatically measured by a Metrohm 856 Conductivity Module (France). The suspensions were titrated using 0.1 M aqueous NaOH (addition rate of 0.1 mL/30 s) [58]. The data were recorded by Tiamo™ Titration software and the conductivity values were corrected from dilution effects and thus plotted against the added volume of sodium hydroxide solution. The inflection point was graphically determined from the intersection of the least squares regression lines fit and the data points in the distinct regions of the titration curves, evaluating the NaOH volume required for neutralization and, thus, the surface charge density [59,60], ρ (mol/g). Using ρ values, the degree of oxidation [61] (DO) was calculated as:

$$DO = \frac{n_{COOH} \times M_{AGU}}{m_{cellulose} - n_{COOH} \times M_{COOH}}$$

where n_{COOH} represents COOH moles (mol) deduced from the surface charge density, ρ; M_{AGU} was the molecular weight of an anhydroglucose unit (162 g/mol); $m_{cellulose}$ corresponded to BCN mass and M_{COOH} was the molecular weight of a carboxylic group.

The zeta potential values were measured using a ZetaSizer Nano ZS (Malvern, UK). BCN suspensions were diluted at 0.1 g/L and filtered (pore diam. = 5 µm). Five measurements at T = 20°C were performed for each sample. For the case of HBCNs suspended in a H_2O/EtOH mixture, the residual ethanol was removed by dialysis of several milliliters of suspension against water for 2 days. All the suspensions were sonicated just before the measurements.

X-ray Absorption Near-Edge Structure (XANES) measurements were performed to investigate the AgNP oxidization state (i.e., metallic silver, Ag_0; ionic silver, Ag^+) while Extended X-ray Absorption Fine Structure (EXAFS) data made it possible to shed light on the AgNP bulk atomic structure (e.g., bond length, interatomic distance). Both XANES and EXAFS spectra were simultaneously recorded in transmission mode at the Ag K-edge (25250 to 27750 eV) on the SAMBA beamline at the SOLEIL synchrotron (Saint Aubin, France). The Si (220) monochromator was calibrated to 25515.6 eV at the first inflection point of the Ag foil XANES spectrum. To be analyzed, all the hybrids were freeze-dried and then compressed to obtain a circular pellet of 6 mm where the quantity of AgNP was high enough to reach an absorption edge jump close to 1. These pellets were placed on a sample rod,

quenched in liquid nitrogen and then introduced into the He cryostat (T = 20 K). Silver foil (Agfoil) and $AgNO_3$ aqueous solution with 1 wt% glycerol (AgH_2O) were used as standards. One continuous scan was recorded for each hybrid sample in the 25250 to 27750 eV energy range with a monochromator velocity of 5 eV/s and an integration time of 0.08 s/point. The obtained scans were then normalized and background-subtracted using the Athena software package [62]. The XANES spectra were analyzed by a linear combination fitting (LCF) procedure in the E_0 - 20 eV, E_0 + 50 eV energy range, with E_0 set to 25514 eV and using Agfoil and AgH_2O standards as components. All component weights were forced to be positive and the relative proportions of the components were forced to add up to 100%. Concerning the EXAFS oscillation, a background subtraction was performed before applying an autobk algorithm (Rbkb = 1, k-weight = 3). The Fourier transform of the k^3-weighted EXAFS spectra was then calculated over a k range of 2.5-19.5 $Å^{-1}$, using a Hanning apodization window (width of the transition region window parameter = 1). The k^3 EXAFS fitting was performed in the 2.35–7.7 Å distance range with the Artemis interface [62] to IFEFFIT using least-squares refinements. Paths used for fitting standards and samples were obtained from a metallic silver crystallographic model [63] using the FEFF6 algorithm included in the Artemis interface. Only paths with a rank higher than 7% were considered, and the E_0 value was set to 25520 eV. The amplitude reduction factor S_0^2 was determined to be equal to 0.978 by fitting the 1st coordination sphere of the Agfoil spectrum over a range of 2.30-2.83 Å. This value was used in all the fitting procedures. Degeneracy of the paths, energy shift ΔE_0, radial distance shift ΔR, and thermal and static disorder σ^2 were fitted for each of the selected paths for a total of 57 independent points and 19 variables. All R-factors were lower than 0.02.

The pellets prepared for XANES-EXAFS measurements were then analyzed by X-ray powder diffraction (XRD). The XRD diffractograms were recorded in 10 min on a Bruker D8 Discover diffractometer (France). Cu-Kα1 radiation (Cu Kα1, 1.5405 Å) produced in a sealed tube at 40 kV and 40 mA was selected and parallelized using a Gobël mirror parallel optics system and collimated to produce a 500-mm beam diameter. The data were collected in the 3°-70° 2θ range. XRD measurements were also performed for initial BCN suspensions with different surface modifications. The crystallinity index (CrI, %) was calculated as a function of the maximum intensity of the diffraction peak from the crystalline region (I_{200}) at 2θ = 22.5° and the minimum intensity from the amorphous region (I_{am}) at 2θ = 18°, according to the Segal equation [64]:

$$\mathrm{CrI} = \frac{I_{200} - I_{am}}{I_{200}}$$

The crystallite size (CS) was determined using Scherrer's equation [65]:

$$CS = \frac{K\lambda}{\beta\cos\theta}$$

where K is the shape factor (0.9), λ is the X-ray wavelength (1.54 Å), β is the full-width at half-maximum (FWHM) and θ is the angle of the diffraction peak of the crystalline phase (Bragg's angle). The FWHM was determined considering the characteristic peak at 2θ = 22.5° for initial BCN suspensions and the peak at 2θ = 38° for the AgNPs in hybrids.

The light-visible absorbance of hybrid suspensions was measured in the 300–800 nm range using a Mettler-Toledo UV7 (USA) spectrophotometer equipped with a 10-mm quartz cell. All the samples were water-diluted (1:10) and ultra-pure water was used as a blank reference.

To determine the real content of AgNPs in hybrid suspensions, a volume of 1 mL of sample was digested by 40 mL water/aqua regia mixture (i.e., 30% v aqua regia, HCl/HNO_3 : 3/1). The resulting suspensions were then analyzed by atomic absorption spectroscopy, AAS (ICE 3300 AAS, Thermo Fisher Scientific, USA). A calibration curve was obtained by the measurement of a digested sample of silver standard solution (1000 µg/mL, Chem-Lab NV, Belgium) at different concentrations, from 0.5 to 10 ppm. Two independent measurements were repeated for each sample.

For scanning transmission electron microscope (STEM) observations, the as-synthesized suspensions were water-diluted at 0.5 g/L in BCN content and 10 µL were then deposited onto glow-discharged carbon coated grids (200 meshes, Delta Microscopies, France) for two minutes, removing the excess by touching the edge of the drop with Whatman filter paper. The grids were dried overnight in air and then coated with a platinum layer (thickness = 0.5 nm) by an ion-sputter coater (LEICA EM ACE600, Germany). Brightfield images were recorded using a field emission gun scanning electron microscope (Quattro S, Thermo Fischer Scientific, USA) operating at 10 kV with a STEM detector. For each sample, the acquired images were analyzed by ImageJ software. The AgNP Feret diameter (i.e., the largest distance between two tangents to the contour of the measured particle) was determined considering the largest possible number of AgNPs (from 35 to 100, depending on the sample).

3. Results

Characteristics of surface-modified BCNs. To elucidate the role of functional groups on the surface of the BCNs in AgNP nucleation, different surface modifications were performed. Firstly, a suspension of neutral BCNs was obtained from HCl acid hydrolysis. BCNs were then carboxylated via the TEMPO oxidation method (TBCN) obtaining a DO of 0.1 estimated from conductometric data. FTIR spectroscopy assessed the effective surface-modifications. As shown in Fig. 2a, the unmodified BCNs showed well-defined peaks at 1000 cm^{-1} and 3000-3500 cm^{-1}, typical of–OH and –C–O–C– groups, respectively [66]. The TBCN spectrum displayed a strong absorption band between 1630 cm^{-1} (carboxylate) and 1730 cm^{-1} (acid), which was characteristic of the carboxyl groups in their acidic form, validating a successful TEMPO oxidation of BCNs [61]. TBCNs were further surface-modified to obtain two types of surface chemistry. Firstly, a cholamine chloride derivative (AETMA) was used

to synthesize aminated cationic BCNs (ABCNs). For this sample, the FTIR spectrum revealed the presence of two new bands at around 1580 cm^{-1} assigned to the C=O stretching of the amide I band and to the N–H vibration of the amide II band, respectively [67]. Secondly, an octylamine C_8 was covalently grafted onto the carboxyl group of TBCNs using NHS/EDC, leading to a hydrophobic BCN (HBCN). The good degree of coupling between TBCNs and C_8 was proved by the very low surface charge density measured by conductometric titration (i.e., 0.010 mmol/g). The detection of these same bands in the spectrum of HBCNs and the presence of asymmetrical and symmetrical CH_2 stretching from the C_8 alkyl chain at 2850 and 2930 cm^{-1} indicated the successful octylamine grafting [43]. Nevertheless, a residual peak at 1730 cm^{-1} was still visible probably due to remaining free COOH groups . FTIR results were corroborated by the variation of the zeta potential (ζ), implying that a modification of the electrical charge environment of the BCN was induced by the different chemical surface modifications. While pure BCNs were quasi-neutral, TBCNs showed a negative ζ value of -25 mV, correlated to the variation of surface charge density (ρ). On the other hand, a clear increase in ζ to +16 mV was observed for the aminated ABCNs due to the substitution of COO^- groups by the N^+ of the AETMA molecules. The slightly negative value of -9 mV was measured for the alkyl hydrophobized HBCNs because of the grafting of octylamine onto the surface carboxyl groups. This low value indicated that HBCNs were highly substituted and no longer electrostatically but, instead, sterically stabilized. These experimental evidences were consistent with a stable suspension of highly-charged colloids for TBCNs and ABCNs with respect to BCNs.

The surface modifications affected the nanocrystal dispersions, as shown from STEM images of dry samples in Fig. 1. Even though the global morphology of the nanocrystals remained unchanged after modification, it could be observed that TBCNs and ABCNs were better dispersed in comparison to quasi-neutral unmodified BCNs and HBCNs. Furthermore, TBCN and ABCN suspensions were less opaque than those of pure BCNs and HBCNs (Fig. 1). Analysis of STEM images indicated an average length of between 850 and 1750 nm and a width of between 20 and 40 nm for all surface-modification treatments, which was in agreement with several studies in the literature [57,68,69]. All the outcomes are summarized in Table 1, indicating that the BCN surface was successfully modified for all of the cases considered.

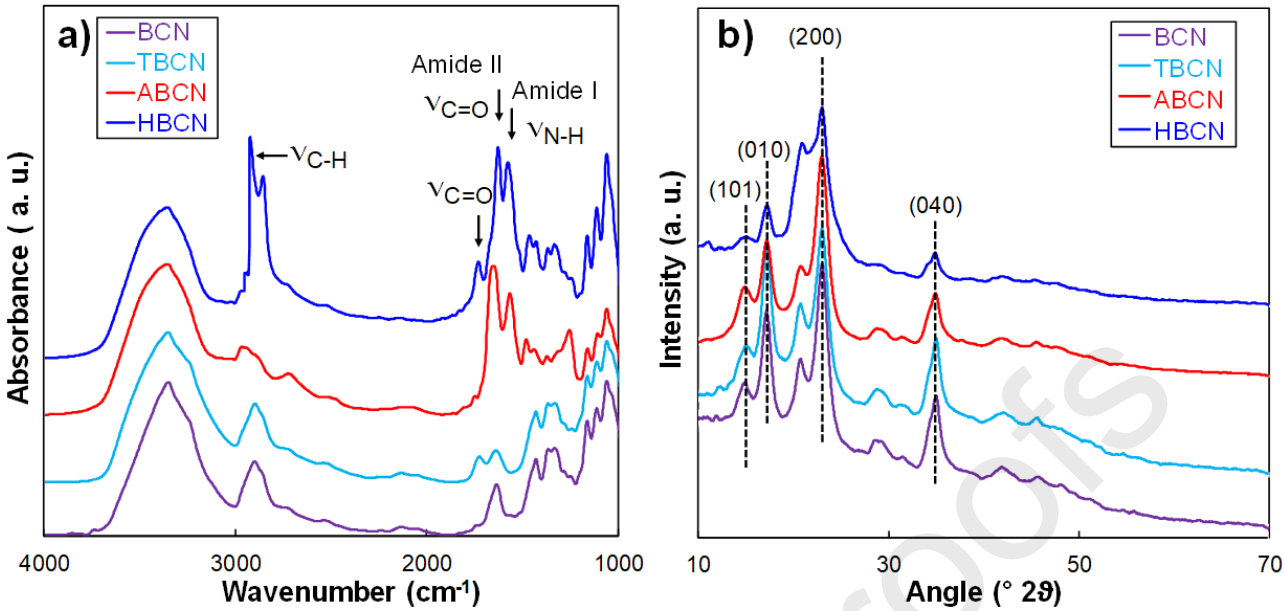

Fig. 2. Characterization of unmodified BCNs and BCNs with TEMPO oxidation, aminated or hydrophobic surface modifications: (a) FTIR spectra; (b) XRD patterns.

Table 1. Crystalline and surface charge characteristics of native and modified BCNs

Sample	Crystallinity, CrI (%)[1]	Crystallite size, CS (nm)[1]	Surface charge density, ρ (mmol/g)[2]	Zeta potential, ζ (mV)
BCN	59	6.1	0.006 ± 0.001	-11.2 ± 1.1
TBCN	57	5.8	0.630 ± 0.003	-25.4 ± 0.8
ABCN	62	5.7	0.540 ± 0.002	+15.9 ± 0.7
HBCN	58	6.1	0.010 ± 0.002	-9.3 ± 1.9

- [1] by XRD; [2] by conductometric titration, two measurements were performed for each sample.

The XRD patterns of unmodified BCNs and surface-modified BCNs (Fig. 2b) showed 2θ diffraction peaks at 14.5°, 16.4°, 22.5° and 34.8°, related to (101), (010), (200) and (040) crystalline planes, respectively, according to the triclinic indexation of Nishiyama et al.[70]. As reported in Table 1, the crystallinity was unchanged around 60% after correction of the amorphous for all the samples, and the chemical treatment did not affect the size of crystallites, which was 5.9 ± 0.2 nm for all the samples, in agreement with the value found by Vasconcelos et al. [71]. These results are consistent with the fact that TEMPO oxidation and other post treatments do not affect the crystalline part of the samples [72,73].

AgNP nucleation on BCNs with various surface modifications. The nucleation of AgNP was investigated on the four BCN types of interest (i.e., native BCNs, TBCNs, ABCNs and HBCNs). Firstly, $AgNO_3$ aqueous solution was added to the BCN suspension and $NaBH_4$ aqueous solution was then introduced to reduce Ag^+ into AgNPs. As soon as the silver precursor was reduced, the initial

translucent aqueous suspension turned light or dark yellow (inset, Fig. 3a), giving different shades of color, probably because of the initial dispersion state of the type of BCN used. However, such a color variation was not reflected in the UV-Vis spectra (Fig. 3a) since the effective AgNP content was very similar in all the hybrids (i.e., 7.9 wt% AgNP in BCN/AgNP; 6.8 wt% AgNP in TBCN/AgNP; 8.5 wt% AgNP in ABCN/AgNP; 8.6 wt% AgNP in HBCN/AgNP) with a same dominant in-plane absorption peak at λ_{max}~ 400 nm. It confirmed the synthesis of well-dispersed AgNPs derived from the coalescence of monomeric Ag particles obtained by a reduction to a zero-valence Ag atom [20].

Even if the surface modification did not seem to affect the intensity of the spectra (i.e., similar AgNP content for all the hybrids), the full width of the main peak and the background intensity increased for HBCN/AgNP. This type of behavior is attributed to the synthesis of HBCN/AgNP in a H_2O/EtOH mixture since the $AgNO_3$ is not well-soluble in ethanol and could affect AgNP nucleation, leading to a larger distribution of AgNP sizes or heterogeneities. However, the use of EtOH was essential since it allowed the C_8 dissolution and helped hydrophobic nanocrystal dispersion after the synthesis, as was the presence of H_2O, which ensured the correct dissolution of silver precursor and, consequently, AgNP formation.

STEM images of dry BCN/AgNP, TBCN/AgNP, ABCN/AgNP and HBCN/AgNP hybrids are shown in Fig. 3b. The analysis of these images confirmed that all the AgNPs had the same particle size, which was thus not affected by the different surface modifications (i.e., BCN/AgNP = 17.1 ± 12 nm; TBCN/AgNP = 17.5 ± 12 nm; ABCN/AgNP = 16.1 ± 13 nm; HBCN/AgNP = 18.0 ± 12 nm). Complete size distributions are reported in Fig. S1. The nucleation growing method resulted in well-grafted AgNPs on the cellulose surface for the neutral and modified CNCs. In contrast, AgNPs synthesized in the same conditions without BCN rapidly aggregated. This proved that BCNs form a perfect substrate for the nucleation point to obtain well-dispersed quite-monodispersed AgNPs without the need for any other capping agents or stabilizers [74].

Nevertheless, these results suggested that AgNP nucleation on the cellulose nanocrystal surface non-specifically occurred on hydroxyl groups and/or on the additional negative surface charges. The aim was to determine if these surface charges represent an additional nucleation point that interacts with Ag^+ ions or if they just acted as promoters of nanocrystal dispersion, facilitating the accessibility to the hydroxyl surface groups. The TEMPO carboxylated TBCNs were then compared to aminated ABCNs. In this case, the functionalization by the positive surface charges preserved the electrostatic repulsion and, consequently, the good dispersion. At the same time, these positive charges could not interact with Ag^+ ions and thus did not represent a possible nucleation point for AgNPs. The STEM image of the ABCN/AgNP hybrid (Fig. 3b) showed that AgNPs were well-nucleated on both surfaces, indicating that the –OH surface groups represented the effective AgNP nucleation point. The OH groups and Ag^+ ions are complexed throught ion-dipole interactions [22] and the extensive number of hydroxyl groups on the BCN surface can promote the complexation of Ag^+ ions also acting as passivation contacts for AgNP stabilization [75].

To our knowledge, such a result represents the first experimental proof that hydroxyl surface groups on cellulosic surfaces are the real nucleation points for metallic nanoparticles and that additional negative surface charges just improve the dispersion state, thereby increasing the accessibility to the nucleation sites. This result was corroborated by the fact that for the HBCN/AgNP hybrid, most of the AgNPs were well-grafted onto the HBCN surface as well. In this case, the only real possible nucleation point was represented by –OH surface groups since most of the carboxylate groups were removed by grafting of C_8 molecules. The presence of several AgNPs not anchored at the HBCN surface was visible in STEM images and could be linked to the suboptimal $AgNO_3$ dissolution due to the presence of EtOH in the suspending medium.

Concerning the structural characterization, all the XRD patterns of BCN/AgNPs (Fig. 3c) showed characteristic peaks of crystalline silver, especially at 37.9° which is usually attributed to the (111) lattice plane of face-centered cubic (fcc) silver (JCPDS Card No. 89-3722). Other characteristic silver diffraction peaks at 46.2° and 64.4° related to other lattice planes (i.e., (200) and (220) crystalline planes) were detected with a weaker intensity. The presence of fcc crystal facets confirmed the isotropic nature of the crystals [20]. For all the samples, the same average AgNP diameter of 3 nm was estimated from XRD patterns. The nucleation mechanism of AgNPs could affect their growth on the nanocrystal surface and, thus, their final characteristics. Therefore, the oxidation state of AgNPs grafted onto BCN with different surface modifications (i.e., Ag_0 and Ag^+ contents) was determined by a linear combination fitting (LCF) of XANES spectra of the hybrids (Fig. S2a and Fig. S2b). For each sample, the R-factor and the Chi-square values of the fits are reported in Table S1. A quantity of 92 ± 9% of Ag_0 was found for all the hybrids, showing the efficiency of the AgNP reduction and nucleation, independently of the surface treatment of the initial BCNs. All Fourier transform spectra of BCN/AgNP (Fig. S2c and Fig. S2d) were fitted with the crystallographic structure of metallic silver with an R-factor systematically lower than 0.015. The shifts in R values (i.e., interatomic distance) obtained from the fits were systematically negligible (< 0.06 $Å^{-1}$; all of the values are presented in Table S2), showing that the interatomic distances in BCN/AgNP case did not significantly change in comparison to the metallic silver distances and that the space group of BCN/AgNP sample still corresponded to the fcc silver structure, as suggested by XRD. It follows that the initial and final crystal structural organization of AgNPs were not affected by the various surface-modification treatments. These results showed the $NaBH_4$ reduction with –OH surface groups as nucleation points represented an efficient nucleation mechanism where the speciation and the crystalline structure of AgNPs were not affected by the surface modifications performed on cellulose nanocrystals.

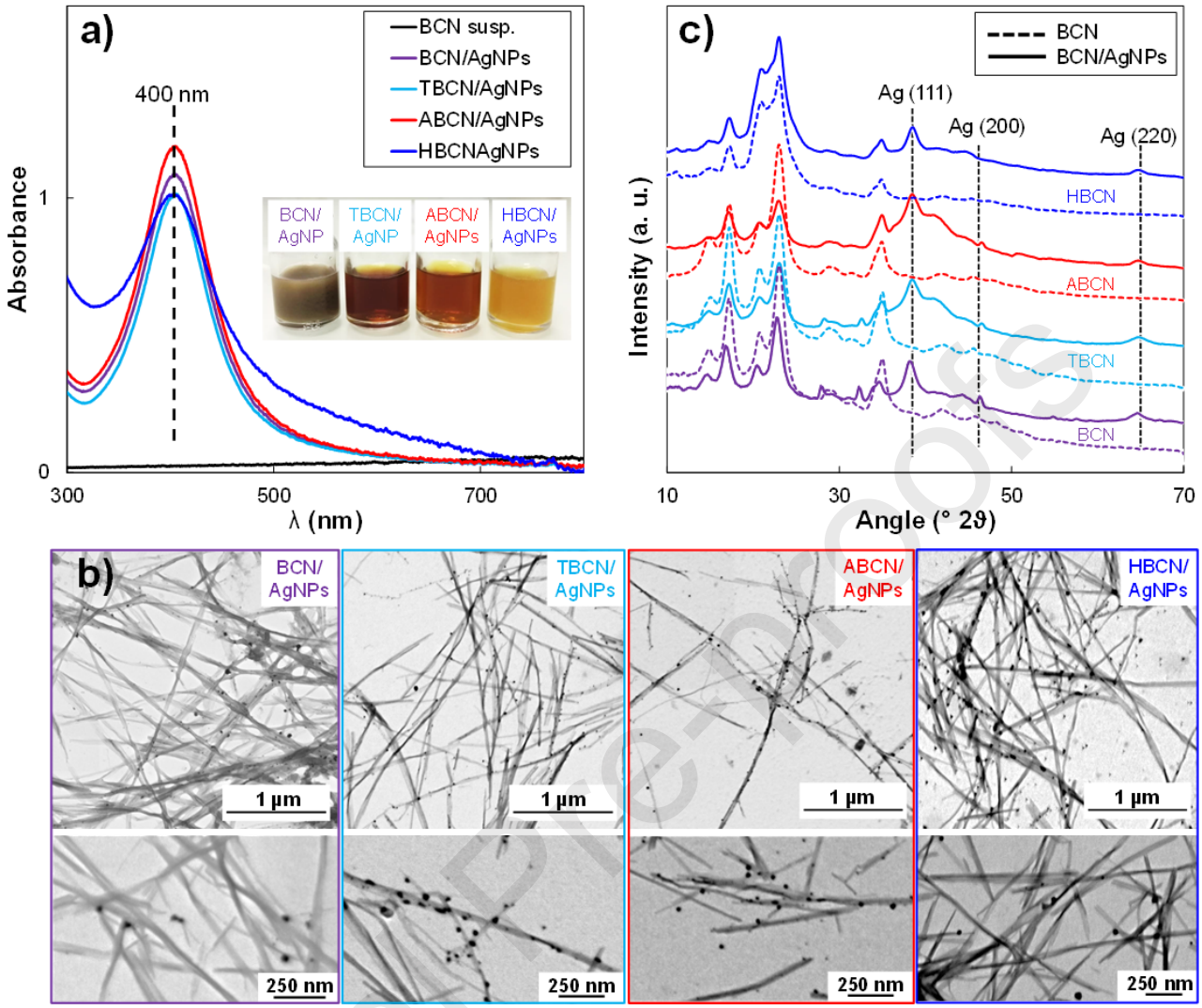

Fig. 3. Characterizations of BCN-, TBCN-, ABCN-, HBCN-/AgNP hybrid suspensions: (a) UV-Vis spectra; inset: sample pictures; (b) STEM images; (c) XRD patterns.

AgNP redox post-treatment by H_2O_2. H_2O_2 was defined as an efficient etching agent producing shape and structural modifications of AgNP into larger and more robust AgNPs (e.g., AgNPrisms) isolated or even attached to surface-carboxylated cellulose nanofibrils [20]. In this case, we proposed a more detailed study on the effect of the H_2O_2 redox post-treatment on properties of AgNPs (i.e., AgNP_H_2O_2) in the different BCN/AgNP hybrids. The outcomes reported in this section will support the understanding of the impact of the H_2O_2 action for BCN/AgNP where BCN was surface-modified. Even if all the prepared samples were able to undergo the same H_2O_2-induced structural change, the TBCN/AgNP hybrid system was chosen as a case study since the TBCNs led to good dispersion. Such a TBCN/AgNP hybrid suspension at constant initial AgNP content (i.e., 7 wt%) was mixed with different amounts of H_2O_2 (40 – 250 µL), thus obtaining a variation of the H_2O_2/AgNP mass ratio, α, from 0 to 0.52, low enough to balance the H_2O_2 oxidative activity and its reduction capability. With the addition of H_2O_2, the color solution drastically changed, ranging from orange to blue (inset, Fig.

4a). The color change was associated with a modification of the UV-Vis spectra of the H_2O_2-containing suspensions with respect to the reference one (i.e., 0 µL H_2O_2), as shown in Fig. 4a. The addition of H_2O_2 induced a redshift of the in-plane dipole surface plasmon resonance peak at 400 nm. This was already visible at α equal to 0.17, since the absorption peak became broader and shifted to 495 nm, showing the presence of two shoulders at 345 nm and 385 nm related to an early modification of primary AgNPs. At α = 0.25, the in-plane plasmon peak was further shifted to 638 nm and finally moved out of the measurement window for higher α values. In this case, a lower intensity peak was detected at λ_{max} = 335 nm that is usually associated with an out-of-plane quadrupole resonance peak, thus representing a good indicator for general prismatic architectures since it strongly depends on aspect ratio [48]. Such a peak became sharper for α values of 0.33 and 0.52 (i.e., 160 µL and 250 µL of H_2O_2, respectively). The presence of a low-intensity peak at 335 nm, at the same time as the shift of the in-plane resonance peak out of the measurement window, and the absence of the primary AgNP peak is proof that an AgNP size-shape variation is induced, as already observed in literature [20]. To better describe the impact of the H_2O_2 redox post-treatment on the AgNP morphology STEM acquisition were performed (Fig. 4b). The analysis of STEM images indicated that AgNPs initially had an average diameter of 17.5 ± 12 nm that regularly increased to reach 94.1 ± 69 nm for α equal to 0.52, where several AgNPs_H_2O_2 with quite irregular edges and a sometimes vaguely triangular shape could be observed. These results agreed with the experimental evidence reported in a recent study of our group [76], in which we investigated the effect of the H_2O_2 redox treatment in hybrid suspensions where primary 10-nm AgNPs are nucleated on wood cellulose NCs, proving the efficient size-shape transition from 10-nm spherical AgNPs into 300 nm AgNPrisms. In this work, we proposed a H_2O_2 redox mechanism where H_2O_2 induced the oxidative dissolution of primary AgNPs, generating Ag^+ ions. When α equal to or greater than 0.20, the H_2O_2 oxidation interest most of the AgNPs, except the contact location where AgNPs are effectively grafted onto the NC surface which could actually work as nucleation sites for the formation of newly formed AgNPs with a triangular shape. Finally, all the images clearly showed that AgNPs_H_2O_2, even the bigger ones, were still attached to the TBCN surface, exactly as for the reference sample before the H_2O_2 post-treatment, showing the importance of cellulose as a support for AgNPs_H_2O_2 nucleation, growth and stabilization. The formation of non-perfectly prismatic silver objects and the increase in the average diameter associated with an increase in the polydispersity in size (Fig. S3a and Fig. S3b, Table S3) could be linked to the absence of any additional stabilizer, which implied that the structural change was heavily affected by the aggregation of newly-formed AgNPs_H_2O_2 [46].

To establish how the H_2O_2 post-treatment affected the oxidation state of AgNPs, XANES spectra were recorded and then fitted using the LCF procedure (Fig. S4a and Table S4). Data showed that the amount of Ag_0 in AgNPs_H_2O_2 slightly decreased with respect to the reference case, from 88% before H_2O_2 post-treatment down to 69% at α = 0.08, as long as the H_2O_2 addition did not induce a size-shape

variation (corresponding to α from 0.08 to 0.25), while remaining equal to 91% and 87% for α values of 0.33 and 0.52, respectively (Table S4). The formation of AgNPs_H_2O_2 mostly composed of Ag_0 silver was also corroborated by the presence in the XRD patterns of characteristic (111), (200) and (220) Ag_0 peaks, confirming the presence of a lattice plane of a face-centered cubic structure (Fig. S4b). It could be observed that the H_2O_2 post-treatment did not induce a structural modification of AgNPs_H_2O_2 with respect to the primary AgNPs before the H_2O_2 treatment and that a H_2O_2/AgNP mass ratio equal to 0.33 and 0.52 determined an increase in the intensity of the characteristic fcc Ag (111) peak, which corresponded to the highest recorded values of Ag_0. Such a result suggested that a α parameter at least equal to 0.33 represented the optimum value necessary to reach an effective size-shape variation that maintains the conversion of the initial Ag^+ to Ag_0 ratio. Finally, the EXAFS Fourier transform spectra (Fig. S4c and Fig. S4d) of the AgNP_H_2O_2 in hybrids were fitted with the crystallographic structure of metallic silver, (R-factor systematically lower than 0.020), presenting systematically negligible shifts in R space (< 0.06 $Å^{-1}$; all values are in Table S5). This result confirmed that the interatomic distances in AgNP_H_2O_2 did not significantly change in comparison to the metallic silver distances and that the space group of the samples still corresponded to the fcc silver structure, as observed by XRD. The final crystal structural organization was not affected by the H_2O_2 redox post-reaction nor by the particle size variation, as observed by Ma et al. [77] Conversely, the AgNP diameter measured by XRD was about 10 nm, which was consistently smaller than the 40-80 nm measured by STEM. Such a difference could be explained by the fact that XRD makes it possible to evaluate the size of the coherent diffraction domains in AgNPs, i.e., perfect repetition in single-crystal particles, twinned or imperfect particles that have more than a single diffraction domain [77]. The characteristics of all the investigated samples are reported in Table 2.

All these results, coupled with the experimental proof that -OH groups on the CNC surface are the AgNP nucleation points, allowed us to conclude that our approach to tune the morphology and the oxidation state of the AgNP grafted onto cellulosic support may be extended to all the hybrid systems where metallic NPs are anchored on a polysaccharide substrate (e.g., cellulose fibers, films or chitin NCs).

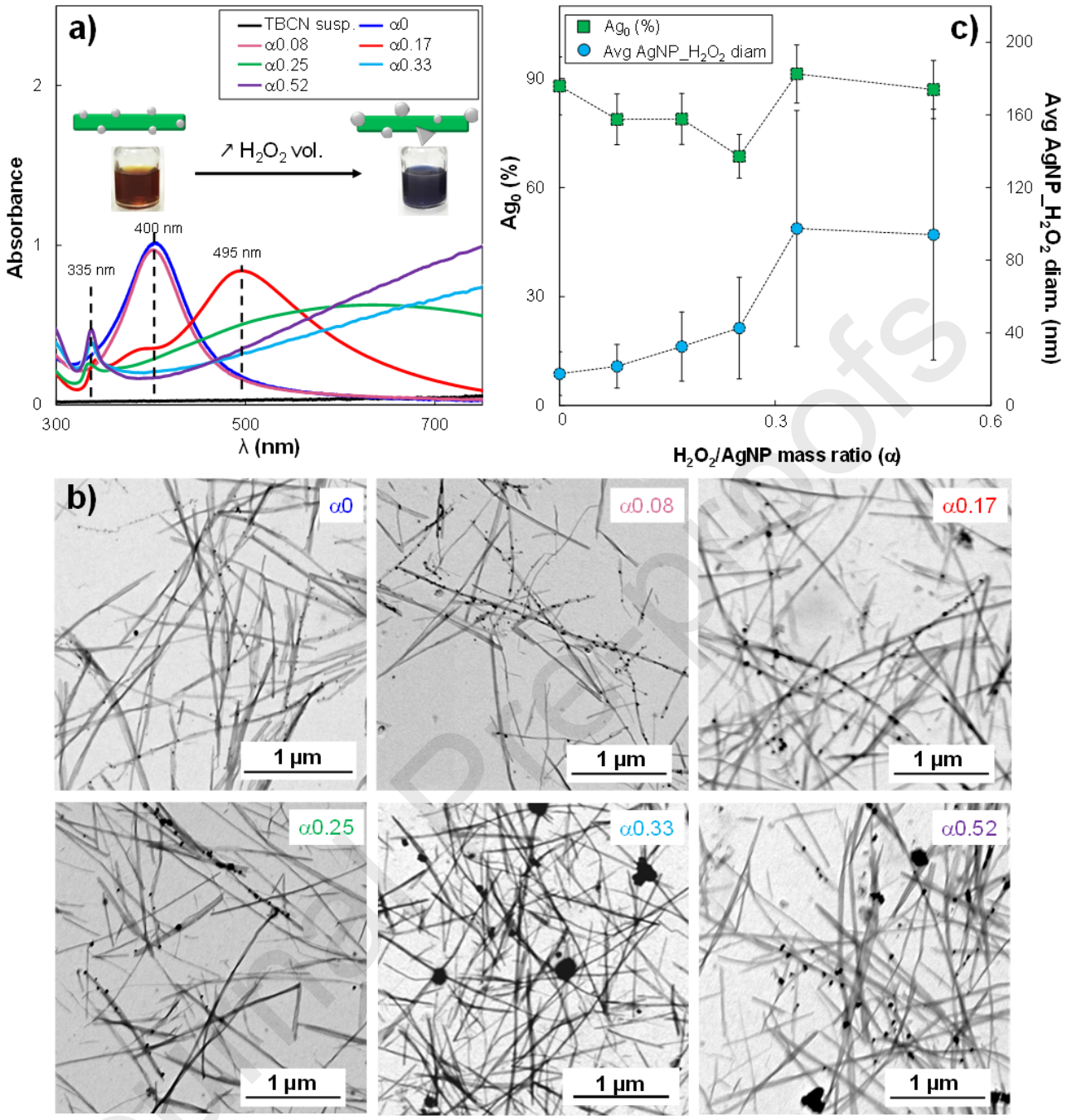

Fig. 4. (a) UV-Vis spectra and (b) STEM images of TBCN/AgNP hybrid suspension mixed with different volumes of H_2O_2 and, thus, at various α values. (c) Ag_0 content of AgNP_H_2O_2 by XANES fitting, and average AgNP_H_2O_2 diameter determined by STEM as a function of the α parameter in TBCN/AgNP_H_2O_2 hybrids. For Ag_0 value, standard error as considered as the 10% of the measured value.

Table 2. Summary of characteristics of BCN/AgNP hybrids with and without H_2O_2 redox post-treatment.

Sample	H_2O_2/AgNP mass ratio (α)	Avg diam. (nm)[1]	Ag_0 (%)[2]
BCN/AgNP	0	17.1 ± 12	90 ± 9

TBCN/AgNP	0	17.5 ± 12	88 ± 9
ABCN/AgNP	0	16.1 ± 13	94 ± 9
HBCN/AgNP	0	18.0 ± 12	97 ± 10
TBCN/AgNP_H_2O_2	0.08	21.6 ± 12	79 ± 8
	0.17	32.5 ± 19	79 ± 8
	0.25	42.7 ± 28	69 ± 7
	0.33	97.5 ± 65	91 ± 9
	0.52	94.1 ± 69	97 ± 10
BCN/AgNP_H_2O_2	0.33	32.5 ± 19	93 ± 9
ABCN/AgNP_H_2O_2	0.33	95.4 ± 87	97 ± 10
HBCN/AgNP_H_2O_2	0.33	29.4 ± 22	97 ± 10

[1] by STEM; [2] by XANES, the standard error as 10% of the measured value.

Impact of BCN surface modification on H_2O_2 redox post-treatment. Hybrids prepared with various BCN types were submitted to the H_2O_2 redox post-treatment, keeping the H_2O_2/AgNP ratio, α, equal to 0.33, the value at which an effective size-shape modification of the initial AgNPs was found in the case of TBCN/AgNP (Table 2). In the case of aminated surfaces, the color variation of the ABCN/AgNP_H_2O_2 from yellow to blue was observed after the addition of H_2O_2, as observed for the TBCN/AgNP_H_2O_2 (Fig. 5a). This suspension showed an in-plane absorption peak shifted to higher λ_{max} (i.e., out of the measurement window), and a sharp out-of-plane quadrupole resonance peak was visible at 333 nm (Fig. 5b). This result agreed with the transformation of the primary AgNPs of 16.1 ± 13 nm into bigger AgNPs_H_2O_2 of 95.4 ± 87 nm, as confirmed by STEM (Fig. 5c). On the other hand, the addition of H_2O_2 to the BCN/AgNP turned the suspension a darker gray color, and the particle size slightly changed with respect to the reference case (i.e., 32.5 ± 19 nm). Moreover, the λ_{max} in the UV-Vis spectra remained at 402 nm and a poorly-defined low-intensity broad peak appeared at 340 nm. These results indicated an uncomplete transformation of the AgNPs, suggesting that the BCN surface modification affected the H_2O_2 transformation of primary AgNPs since the BCN surface modification influenced the BCN dispersion rather than its chemical structure.

When the surface charges provided a good repulsion between nanocrystals (the cases of TBCN and ABCN), the addition of H_2O_2 made it possible to obtain the formation of AgNPs_H_2O_2 of about 100 nm, whereas the size of AgNPs_H_2O_2 for the almost neutral surface charge in the BCN case remained constant (i.e., about 20 nm). It appeared that well-dispersed nanocrystals facilitate the accessibility to the surface groups, thereby promoting the H_2O_2 redox action.

Concerning the hydrophobically-modified surface (i.e., HBCN/AgNP case), the introduction of H_2O_2 did not induce a size-shape modification of primary AgNPs, as shown in the STEM image (Fig. 5c).

Furthermore, the UV-Vis spectrum of the HBCN/AgNP_H_2O_2 suspension did not change with respect to the reference HBCN/AgNP. In this case, not only the absence of repulsion prevented good nanocrystal dispersion, but the suspending medium containing EtOH could promote aggregation and affect the efficiency of the H_2O_2 redox reaction as well. To check the influence of EtOH on the H_2O_2 treatment, we compared aqueous TBCN/AgNPs suspension (highly charged nanocrystals to ensure dispersion) to the same TBCN/AgNPs diluted in a H_2O/EtOH (60/40 v/v) mixture, like in the case of the HBCN/AgNPs. In pure water, the addition of H_2O_2 induced a color variation from yellow to blue, whereas the hybrid prepared in the H_2O/EtOH mixture just turned a dark yellow (Fig. S5). This result confirmed that the presence of ethanol limited the formation of AgNPs_H_2O_2 that could be linked to a weak oxidation of AgNPs to Ag^+ and the subsequent reduction in a non-aqueous medium. Size distributions of AgNPs_H_2O_2 in BCN hybrids are reported in Fig. S6 and the average diameters are summarized in Table S6.

Interestingly, all the reformed AgNPs_H_2O_2 appeared to be nucleated on nanocrystal surfaces, irrespective of the applied surface modification. This means that the BCN still serves as a substrate for AgNP_H_2O_2 formation, ensuring adequate AgNP dispersion. We hypothesized that the H_2O_2 did not completely oxidize the AgNPs, leaving hooks available as a large amount of re-nucleation points for AgNP_H_2O_2 nanoparticles in addition to the –OH surface groups, as reported in another work of our group [76].

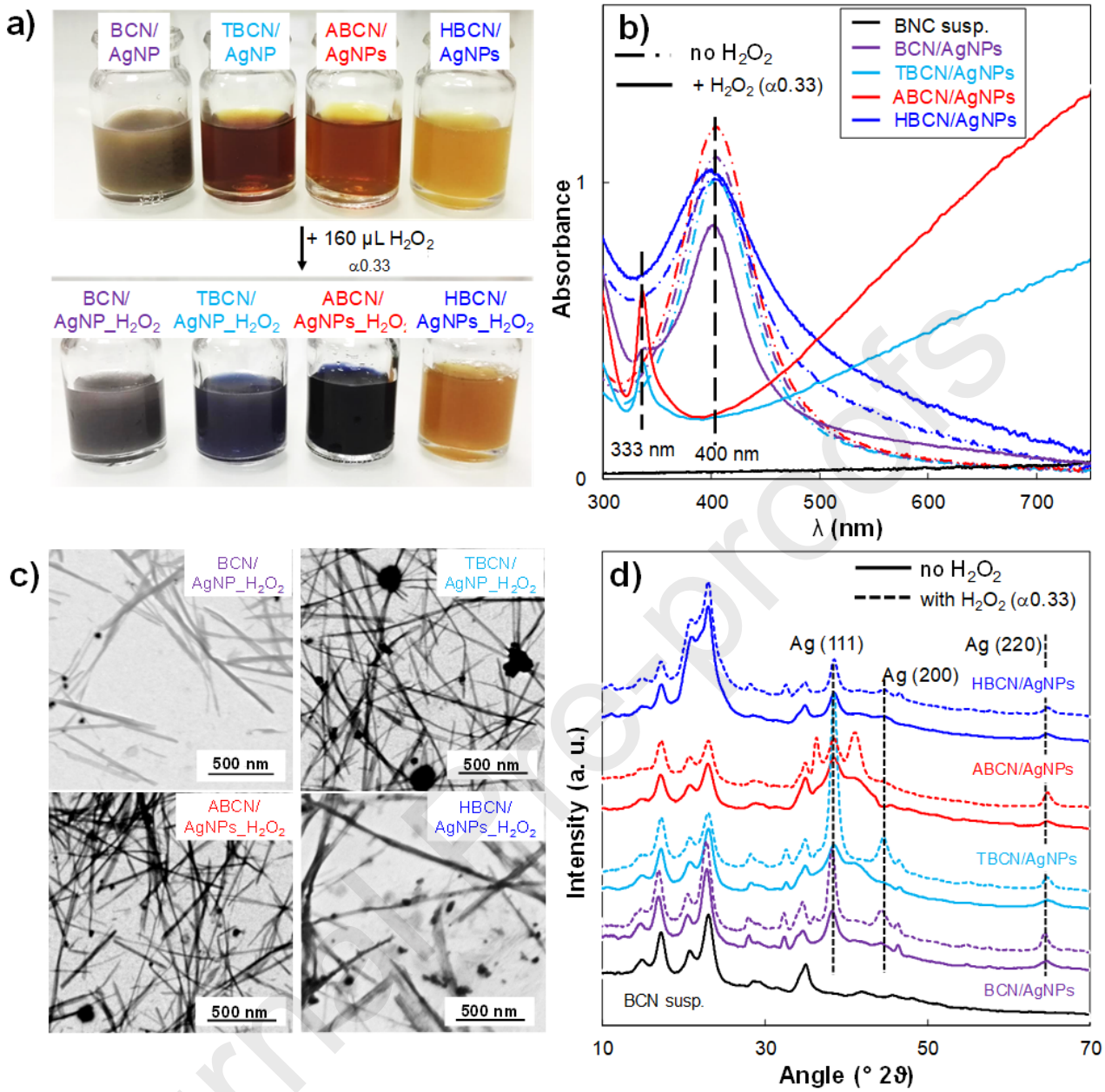

Fig. 5. (a) Color variation of hybrid suspensions; (b) UV-Vis spectra; (c) STEM images; (d) XRD patterns of BCN-, TBCN-, ABCN-, HBCN-/AgNP_H_2O_2 hybrid suspensions with the addition of 160 µL of H_2O_2 (α = 0.33).

Moreover, the analysis of XANES spectra (Fig. S7a, Table S7) showed that the addition of H_2O_2 did not affect the Ag_0 content (i.e., 95 ± 10% compared to 92 ± 9% of the reference cases), indicating that the oxidation state did not change. Finally, the XRD patterns of hybrid suspensions without (α = 0) and with the addition of H_2O_2 (α = 0.33), Fig. 5d., indicating the presence of the Ag (111), Ag (200) and Ag (220) peaks, characteristic of the fcc silver model. This confirmed the formation of metallic AgNPs_H_2O_2 well-grafted onto the BCN substrate, irrespective of the surface modification. Moreover, the fitting of EXAFS Fourier transform spectra (R-factor < 0.016) did not reveal any significant modification of the crystallographic structure in comparison to fcc metallic silver (Fig. S8a and Fig.

S8b, data in Table S8). These studies confirmed that all native and modified BCN/AgNP samples were composed quasi-exclusively of Ag_0 with similar crystallographic organization.

4. Conclusion

In this study, we investigated the interactions involving well-dispersed AgNPs grafted on a bio-based substrate, focusing on the role of polysaccharide surface chemistry. Working with bacterial cellulose nanocrystals (BCNs) as model substrate, we experimentally showed that the hydroxyl groups serve as nucleation points for AgNPs through ion-dipole interaction and that the surface charges only promoted nanocrystal dispersion, improving accessibility to the OH groups. To our knowledge, this is the first experimental identification of the effective nucleation point for metallic nanoparticles on a solid cellulose surface. This was investigated modifying native quasi-neutral BCNs dispersed in aqueous suspension into negatively or positively charged, and hydrophobic BCNs then used to prepare hybrid nanomaterials (i.e., BCN/AgNP, TBCN/AgNP, ABCN/AgNP, HBCN/AgNP) where highly controlled AgNPs are anchored on the BCN surface. This work proved that no surface modification of cellulose (e.g., TEMPO oxidation [32]) is necessary to efficiently nucleate and anchor AgNPs on their surface as long as the reduction step is carried out. Furthermore, we prove that the grafting of hydrophobic molecules on BCNs does not prevent the nucleation and the growth of AgNPs, thus opening the way to the formulation of bifunctional nanoparticles in non-aqueous media.

The investigated hybrid suspensions were subjected to an H_2O_2 redox post-treatment. An optimal H_2O_2/AgNP mass ratio ($\alpha = 0.33$) was defined at which a size-shape transition of AgNPs, from 10-nm spherical NPs to 100-nm NPs with a triangular shape, while maintaining the initial fcc crystal structure and increasing the Ag_0 content in AgNPs. Here, we showed that the dispersion of the BCNs improved the efficiency of the H_2O_2 post-treatment, with an increase in AgNP size detected only in presence of repulsive surface charges (i.e., TBCNs and ABCNs)

As a result, this highly controlled synthesis of AgNPs well-grafted onto the cellulose NC surface can promote the development and design of new bio-based hybrid materials, such as sensors and biological imaging, catalysts, conductive material. Furthermore, a controlled release of Ag^+ ions from well-characterized AgNPs would allow producing bio-based nanomaterials for biocidal properties that can be used for several applications, such as food packaging, paints or surface treatment.

CRediT authorship contribution statement

D. Musino: Conceptualization, methodology, investigation, formal analysis, visualization, data curation, writing – original draft. **C. Rivard:** Formal analysis, investigation, writing – review and editing. **G. Landrot:** Formal analysis, investigation, writing – review and editing. **B. Novales:** Investigation, writing – review and editing. **T. Rabilloud:** Supervision, investigation, writing – review and editing. **I.Capron:** Conceptualization, investigation, supervision, project administration, writing - review & editing.

Declaration of competing interest

The authors declare that they have no known competing financial interests or personal relationships that could have appeared to influence the work reported in this paper;

Acknowledgments

We acknowledge SOLEIL for providing synchrotron radiation facilities on the SAMBA beamline. We are grateful to S. Durand (BIA-Nantes) for her support with FTIR measurements, F. X. Lefevre and N. Guichard (Université de Nantes) for their support with AAS experiments, B. Pontoire (BIA-Nantes) for performing XRD acquisitions, and S. Haouache (BIA-Nantes) for her assistance during SAMBA beam time. This work is a contribution to the Labex SERENADE (n° ANR-11-LABX-0064), funded by the "Investissement d'Avenir" French government program of the French National Research Agency (ANR) through the A*MIDEX project (n° ANR-11-IDEX-0001-02).

Appendix A. Supplementary data

Supplementary data to this article can be found online at: 10.1016/x0xx00000x

References

[1] E. Board, L.T.E. Long, T.B. Voit, Polyscaccharides II, 2006. https://doi.org/10.1007/978-3-540-85103-5.

[2] S. Iwamoto, A.N. Nakagaito, H. Yano, M. Nogi, Optically transparent composites reinforced with plant fiber-based nanofibers, Appl. Phys. A Mater. Sci. Process. 81 (2005) 1109–1112. https://doi.org/10.1007/s00339-005-3316-z.

[3] I. Siró, D. Plackett, Microfibrillated cellulose and new nanocomposite materials: A review, Cellulose. 17 (2010) 459–494. https://doi.org/10.1007/s10570-010-9405-y.

[4] P. Ross, R. Mayer, M. Benziman, Cellulose biosynthesis and function in bacteria., Microbiol. Rev. 55 (1991) 35–58. http://www.ncbi.nlm.nih.gov/pubmed/2030672%0Ahttp://www.pubmedcentral.nih.gov/articlerender.fcgi?artid=PMC372800.

[5] W. Czaja, A. Krystynowicz, S. Bielecki, R.M. Brown, Microbial cellulose - The natural power to heal wounds, Biomaterials. 27 (2006) 145–151. https://doi.org/10.1016/j.biomaterials.2005.07.035.

[6] Y. Hu, J.M. Catchmark, Y. Zhu, N. Abidi, X. Zhou, J. Wang, N. Liang, Engineering of porous bacterial cellulose toward human fibroblasts ingrowth for tissue engineering, J. Mater. Res. 29 (2014) 2682–2693. https://doi.org/10.1557/jmr.2014.315.

[7] A. Svensson, E. Nicklasson, T. Harrah, B. Panilaitis, D.L. Kaplan, M. Brittberg, P. Gatenholm, Bacterial cellulose as a potential scaffold for tissue engineering of cartilage, Biomaterials. 26 (2005) 419–431. https://doi.org/10.1016/j.biomaterials.2004.02.049.

[8] P. Boonme, Amnuaikit, Chusuit, Raknam, Effects of a cellulose mask synthesized by a bacterium on facial skin characteristics and user satisfaction, Med. Devices Evid. Res. (2011) 77. https://doi.org/10.2147/mder.s20935.

[9] K.C. Cheng, J.M. Catchmark, A. Demirci, Effects of CMC addition on bacterial cellulose production in a biofilm reactor and its paper sheets analysis, Biomacromolecules. 12 (2011) 730–736. https://doi.org/10.1021/bm101363t.

[10] S. Eyley, W. Thielemans, Surface modification of cellulose nanocrystals, Nanoscale. 6 (2014) 7764–7779. https://doi.org/10.1039/c4nr01756k.

[11] D. Klemm, F. Kramer, S. Moritz, T. Lindström, M. Ankerfors, D. Gray, A. Dorris, Nanocelluloses: A new family of nature-based materials, Angew. Chemie - Int. Ed. 50 (2011) 5438–5466. https://doi.org/10.1002/anie.201001273.

[12] J. Ramyadevi, K. Jeyasubramanian, A. Marikani, G. Rajakumar, A.A. Rahuman, Synthesis and antimicrobial activity of copper nanoparticles, Mater. Lett. 71 (2012) 114–116. https://doi.org/10.1016/j.matlet.2011.12.055.

[13] V.K. Sharma, R.A. Yngard, Y. Lin, Silver nanoparticles: green synthesis and their antimicrobial activities., Adv. Colloid Interface Sci. 145 (2009) 83–96. https://doi.org/10.1016/j.cis.2008.09.002.

[14] S. Gunalan, R. Sivaraj, V. Rajendran, Green synthesized ZnO nanoparticles against bacterial and fungal pathogens, Prog. Nat. Sci. Mater. Int. 22 (2012) 693–700. https://doi.org/10.1016/j.pnsc.2012.11.015.

[15] X. Li, S.M. Robinson, A. Gupta, K. Saha, Z. Jiang, D.F. Moyano, A. Sahar, M.A. Riley, V.M. Rotello, Functional gold nanoparticles as potent antimicrobial agents against multi-drug-resistant bacteria, ACS Nano. 8 (2014) 10682–10686. https://doi.org/10.1021/nn5042625.

[16] R.J.B. Pinto, P.A.A.P. Marques, C.P. Neto, T. Trindade, S. Daina, P. Sadocco, Antibacterial activity of nanocomposites of silver and bacterial or vegetable cellulosic fibers, Acta Biomater. 5 (2009) 2279–2289. https://doi.org/10.1016/j.actbio.2009.02.003.

[17] C.H. Bae, S.H. Nam, S.M. Park, Formation of silver nanoparticles by laser ablation of a silver target in NaCl solution, Appl. Surf. Sci. 197–198 (2002) 628–634. https://doi.org/10.1016/S0169-4332(02)00430-0.

[18] U. Nickel, A.Z. Castell, K. Pöppl, S. Schneider, Silver colloid produced by reduction with hydrazine as support for highly sensitive surface-enhanced Raman spectroscopy, Langmuir. 16 (2000) 9087–9091. https://doi.org/10.1021/la000536y.

[19] G. Yang, J. Xie, F. Hong, Z. Cao, X. Yang, Antimicrobial activity of silver nanoparticle impregnated bacterial cellulose membrane: Effect of fermentation carbon sources of bacterial cellulose, Carbohydr. Polym. 87 (2012) 839–845. https://doi.org/10.1016/j.carbpol.2011.08.079.

[20] F. Jiang, Y. Lo Hsieh, Synthesis of cellulose nanofibril bound silver nanoprism for surface

enhanced raman scattering, Biomacromolecules. 15 (2014) 3608–3616. https://doi.org/10.1021/bm5011799.

[21] M. Tsuji, S. Gomi, Y. Maeda, M. Matsunaga, S. Hikino, K. Uto, T. Tsuji, H. Kawazumi, Rapid transformation from spherical nanoparticles, nanorods, cubes, or bipyramids to triangular prisms of silver with PVP, citrate, and H 2O 2, Langmuir. 28 (2012) 8845–8861. https://doi.org/10.1021/la3001027.

[22] A.R. Lokanathan, K.M.A. Uddin, O.J. Rojas, J. Laine, Cellulose nanocrystal-mediated synthesis of silver nanoparticles: Role of sulfate groups in nucleation phenomena, Biomacromolecules. 15 (2014) 373–379. https://doi.org/10.1021/bm401613h.

[23] D.L. Van Hyning, C.F. Zukoski, Formation Mechanisms and Aggregation Behavior of Borohydride Reduced Silver Particles, Langmuir. 14 (2002) 7034–7046. https://doi.org/10.1021/la980325h.

[24] G. Ling, J. He, L. Huang, Size control of silver nanoparticles deposited on silica dielectric spheres by electroless plating technique, J. Mater. Sci. 39 (2004) 2955–2957. https://doi.org/10.1023/b:jmsc.0000021490.52788.62.

[25] Y. Qin, X. Ji, J. Jing, H. Liu, H. Wu, W. Yang, Size control over spherical silver nanoparticles by ascorbic acid reduction, Colloids Surfaces A Physicochem. Eng. Asp. 372 (2010) 172–176. https://doi.org/10.1016/j.colsurfa.2010.10.013.

[26] Y. Sun, B. Mayers, Y. Xia, Transformation of silver nanospheres into nanobelts and triangular nanoplates through a thermal process, Nano Lett. 3 (2003) 675–679. https://doi.org/10.1021/nl034140t.

[27] S. Padalkar, J.R. Capadona, S.J. Rowan, C. Weder, Y.H. Won, L.A. Stanciu, R.J. Moon, Natural biopolymers: Novel templates for the synthesis of nanostructures, Langmuir. 26 (2010) 8497–8502. https://doi.org/10.1021/la904439p.

[28] K. Patel, B. Bharatiya, T. Mukherjee, T. Soni, A. Shukla, B.N. Suhagia, Role of stabilizing agents in the formation of stable silver nanoparticles in aqueous solution: Characterization and stability study, J. Dispers. Sci. Technol. 38 (2017) 626–631. https://doi.org/10.1080/01932691.2016.1185374.

[29] M. Kaushik, A. Moores, Review: Nanocelluloses as versatile supports for metal nanoparticles and their applications in catalysis, Green Chem. 18 (2016) 622–637. https://doi.org/10.1039/c5gc02500a.

[30] R. Xiong, C. Lu, W. Zhang, Z. Zhou, X. Zhang, Facile synthesis of tunable silver nanostructures for antibacterial application using cellulose nanocrystals, Carbohydr. Polym. 95 (2013) 214–219. https://doi.org/10.1016/j.carbpol.2013.02.077.

[31] H. Dong, J.F. Snyder, D.T. Tran, J.L. Leadore, Hydrogel, aerogel and film of cellulose nanofibrils functionalized with silver nanoparticles, Carbohydr. Polym. 95 (2013) 760–767. https://doi.org/10.1016/j.carbpol.2013.03.041.

[32] S. Ifuku, M. Tsuji, M. Morimoto, H. Saimoto, H. Yano, Synthesis of silver nanoparticles templated by TEMPO-mediated oxidized bacterial cellulose nanofibers, Biomacromolecules. 10 (2009) 2714–2717. https://doi.org/10.1021/bm9006979.

[33] L. Johnson, W. Thielemans, D.A. Walsh, Nanocomposite oxygen reduction electrocatalysts formed using bioderived reducing agents, J. Mater. Chem. 20 (2010) 1737–1743. https://doi.org/10.1039/b922423h.

[34] M. Hasani, E.D. Cranston, G. Westman, D.G. Gray, Cationic surface functionalization of cellulose nanocrystals, Soft Matter. 4 (2008) 2238–2244. https://doi.org/10.1039/b806789a.

[35] H. Rosilo, J.R. McKee, E. Kontturi, T. Koho, V.P. Hytönen, O. Ikkala, M.A. Kostiainen, Cationic polymer brush-modified cellulose nanocrystals for high-affinity virus binding, Nanoscale. 6 (2014) 11871–11881. https://doi.org/10.1039/c4nr03584d.

[36] A. Kaboorani, B. Riedl, Surface modification of cellulose nanocrystals (CNC) by a cationic surfactant, Ind. Crops Prod. 65 (2015) 45–55. https://doi.org/10.1016/j.indcrop.2014.11.027.

[37] S. Lombardo, W. Thielemans, Thermodynamics of the interactions of positively charged cellulose nanocrystals with molecules bearing different amounts of carboxylate anions, Phys. Chem. Chem. Phys. 20 (2018) 17637–17647. https://doi.org/10.1039/c8cp01532e.

[38] L. Jasmani, S. Eyley, R. Wallbridge, W. Thielemans, A facile one-pot route to cationic cellulose nanocrystals, Nanoscale. 5 (2013) 10207–10211. https://doi.org/10.1039/c3nr03456a.

[39] M. Shateri Khalil-Abad, M.E. Yazdanshenas, M.R. Nateghi, Effect of cationization on adsorption of silver nanoparticles on cotton surfaces and its antibacterial activity, Cellulose. 16 (2009) 1147–1157. https://doi.org/10.1007/s10570-009-9351-8.

[40] B.H. Dong, J.P. Hinestroza, Metal nanoparticles on natural cellulose fibers: Electrostatic assembly and in situ synthesis, ACS Appl. Mater. Interfaces. 1 (2009) 797–803. https://doi.org/10.1021/am800225j.

[41] J. Araki, M. Wada, S. Kuga, Steric stabilization of a cellulose microcrystal suspension by poly(ethylene glycol) grafting, Langmuir. 17 (2001) 21–27. https://doi.org/10.1021/la001070m.

[42] Y. Zhang, V. Karimkhani, B.T. Makowski, G. Samaranayake, S.J. Rowan, Nanoemulsions and Nanolatexes Stabilized by Hydrophobically Functionalized Cellulose Nanocrystals, Macromolecules. 50 (2017) 6032–6042. https://doi.org/10.1021/acs.macromol.7b00982.

[43] Z. Hu, R.M. Berry, R. Pelton, E.D. Cranston, One-Pot Water-Based Hydrophobic Surface Modification of Cellulose Nanocrystals Using Plant Polyphenols, ACS Sustain. Chem. Eng. 5 (2017) 5018–5026. https://doi.org/10.1021/acssuschemeng.7b00415.

[44] A.G. Cunha, J.B. Mougel, B. Cathala, L.A. Berglund, I. Capron, Preparation of double pickering emulsions stabilized by chemically tailored nanocelluloses, Langmuir. 30 (2014) 9327–9335. https://doi.org/10.1021/la5017577.

[45] J.E. Millstone, S.J. Hurst, G.S. Métraux, J.I. Cutler, C.A. Mirkin, Colloidal gold and silver triangular nanoprisms, Small. 5 (2009) 646–664. https://doi.org/10.1002/smll.200801480.

[46] T. Parnklang, B. Lamlua, H. Gatemala, C. Thammacharoen, S. Kuimalee, B. Lohwongwatana, S. Ekgasit, Shape transformation of silver nanospheres to silver nanoplates induced by redox reaction of hydrogen peroxide, Mater. Chem. Phys. 153 (2015) 127–134. https://doi.org/10.1016/j.matchemphys.2014.12.044.

[47] G.S. Métraux, C.A. Mirkin, Rapid thermal synthesis of silver nanoprisms with chemically tailorable thickness, Adv. Mater. 17 (2005) 412–415. https://doi.org/10.1002/adma.200401086.

[48] R. Jin, Y. Cao, C. Mirkin, K. Kelly, G. Schatz, J. Zheng, Photoinduced Conversion of Silver Nanospheres to Nanoprisms, 1901 (2013) 1901–1904. https://doi.org/10.1126/science.1066541.

[49] S. Chen, D.L. Carroll, For Evaluation Only . Synthesis and Characterization of Truncated Triangular Silver Nanoplates, Nano. (2008) 2005–2008.

[50] A.J. Haes, R.P. Van Duyne, A nanoscale optical biosensor: Sensitivity and selectivity of an approach based on the localized surface plasmon resonance spectroscopy of triangular silver nanoparticles, J. Am. Chem. Soc. 124 (2002) 10596–10604. https://doi.org/10.1021/ja020393x.

[51] A.D. McFarland, R.P. Van Duyne, Single silver nanoparticles as real-time optical sensors with zeptomole sensitivity, Nano Lett. 3 (2003) 1057–1062. https://doi.org/10.1021/nl034372s.

[52] K.A. Homan, M. Souza, R. Truby, G.P. Luke, C. Green, E. Vreeland, S. Emelianov, Silver nanoplate contrast agents for in vivo molecular photoacoustic imaging, ACS Nano. 6 (2012) 641–650. https://doi.org/10.1021/nn204100n.

[53] P. Christopher, S. Linic, Engineering selectivity in heterogeneous catalysis: The impact of Ag surface structure on ethylene epoxidation selectivity, AIChE Annu. Meet. Conf. Proc. (2008) 11264–11265.

[54] A.P. Kulkarni, K.M. Noone, K. Munechika, S.R. Guyer, D.S. Ginger, Plasmon-enhanced charge carrier generation in organic photovoltaic films using silver nanoprisms, Nano Lett. 10 (2010) 1501–1505. https://doi.org/10.1021/nl100615e.

[55] C. Yang, H. Gu, W. Lin, M.M. Yuen, C.P. Wong, M. Xiong, B. Gao, Silver nanowires: From scalable synthesis to recyclable foldable electronics, Adv. Mater. 23 (2011) 3052–3056. https://doi.org/10.1002/adma.201100530.

[56] X. Lin, M. Wu, D. Wu, S. Kuga, T. Endo, Y. Huang, Platinum nanoparticles using wood nanomaterials: Eco-friendly synthesis, shape control and catalytic activity for p-nitrophenol reduction, Green Chem. 13 (2011) 283–287. https://doi.org/10.1039/c0gc00513d.

[57] I. Kalashnikova, H. Bizot, B. Cathala, I. Capron, New pickering emulsions stabilized by bacterial cellulose nanocrystals, Langmuir. 27 (2011) 7471–7479. https://doi.org/10.1021/la200971f.

[58] J. Araki, Y. Hida, Comparison of methods for quantitative determination of silver content in cellulose nanowhisker/silver nanoparticle hybrids, Cellulose. 25 (2018) 1065–1076. https://doi.org/10.1007/s10570-017-1640-z.

[59] S. Beck, M. Méthot, J. Bouchard, General procedure for determining cellulose nanocrystal sulfate half-ester content by conductometric titration, Cellulose. 22 (2015) 101–116. https://doi.org/10.1007/s10570-014-0513-y.

[60] T. Abitbol, E. Kloser, D.G. Gray, Estimation of the surface sulfur content of cellulose nanocrystals prepared by sulfuric acid hydrolysis, Cellulose. 20 (2013) 785–794. https://doi.org/10.1007/s10570-013-9871-0.

[61] D. da Silva Perez, S. Montanari, M.R. Vignon, TEMPO-mediated oxidation of cellulose III, Biomacromolecules. 4 (2003) 1417–1425. https://doi.org/10.1021/bm034144s.

[62] B. Ravel, M. Newville, ATHENA, ARTEMIS, HEPHAESTUS: Data analysis for X-ray absorption spectroscopy using IFEFFIT, J. Synchrotron Radiat. 12 (2005) 537–541. https://doi.org/10.1107/S0909049505012719.

[63] I.K. Suh, H. Ohta, Y. Waseda, High-temperature thermal expansion of six metallic elements measured by dilatation method and X-ray diffraction, J. Mater. Sci. 23 (1988) 757–760. https://doi.org/10.1007/BF01174717.

[64] L. Segal, J.J. Creely, A.E. Martin, C.M. Conrad, An Empirical Method for Estimating the Degree of Crystallinity of Native Cellulose Using the X-Ray Diffractometer, Text. Res. J. 29 (1959) 786–794. https://doi.org/10.1177/004051755902901003.

[65] P. Singhsa, R. Narain, H. Manuspiya, Bacterial Cellulose Nanocrystals (BCNC) Preparation and Characterization from Three Bacterial Cellulose Sources and Development of Functionalized BCNCs as Nucleic Acid Delivery Systems, ACS Appl. Nano Mater. 1 (2018) 209–221. https://doi.org/10.1021/acsanm.7b00105.

[66] N.M. Girouard, S. Xu, G.T. Schueneman, M.L. Shofner, J.C. Meredith, Site-Selective Modification of Cellulose Nanocrystals with Isophorone Diisocyanate and Formation of Polyurethane-CNC Composites, ACS Appl. Mater. Interfaces. 8 (2016) 1458–1467. https://doi.org/10.1021/acsami.5b10723.

[67] T. Miyazawa, T. Shimanouchi, S.I. Mizushima, Characteristic infrared bands of monosubstituted amides, J. Chem. Phys. 24 (1956) 408–418. https://doi.org/10.1063/1.1742489.

[68] J. Araki, M. Wada, S. Kuga, T. Okano, Flow properties of microcrystalline cellulose suspension prepared by acid treatment of native cellulose, Colloids Surfaces A Physicochem. Eng. Asp. 142 (1998) 75–82. https://doi.org/10.1016/S0927-7757(98)00404-X.

[69] Y. Habibi, L.A. Lucia, O.J. Rojas, Cellulose Nanocrystals: Chemistry, Self-Assembly, and Applications, Chem. Rev. 110 (2010) 3479–3500. https://doi.org/10.1021/cr900339w.

[70] Y. Nishiyama, J. Sugiyama, H. Chanzy, P. Langan, Crystal Structure and Hydrogen Bonding System in Cellulose Iα from Synchrotron X-ray and Neutron Fiber Diffraction, J. Am. Chem. Soc. 125 (2003) 14300–14306. https://doi.org/10.1021/ja037055w.

[71] N.F. Vasconcelos, J.P.A. Feitosa, F.M.P. da Gama, J.P.S. Morais, F.K. Andrade, M. de S.M. de

Souza Filho, M. de F. Rosa, Bacterial cellulose nanocrystals produced under different hydrolysis conditions: Properties and morphological features, Carbohydr. Polym. 155 (2017) 425–431. https://doi.org/10.1016/j.carbpol.2016.08.090.

[72] T. Saito, A. Isogai, TEMPO-mediated oxidation of native cellulose. The effect of oxidation conditions on chemical and crystal structures of the water-insoluble fractions, Biomacromolecules. 5 (2004) 1983–1989. https://doi.org/10.1021/bm0497769.

[73] Y. Okita, T. Saito, A. Isogai, Entire Surface Oxidation of Various Cellulose Microfibrils by TEMPO-Mediated Oxidation, Biomacromolecules. 11 (2010) 1696–1700. https://doi.org/10.1021/bm100214b.

[74] J.Y. Song, B.S. Kim, Rapid biological synthesis of silver nanoparticles using plant leaf extracts., Bioprocess Biosyst. Eng. 32 (2009) 79–84. https://doi.org/10.1007/s00449-008-0224-6.

[75] P. Raveendran, J. Fu, S.L. Wallen, Completely "Green" Synthesis and Stabilization of Metal Nanoparticles, J. Am. Chem. Soc. 125 (2003) 13940–13941. https://doi.org/10.1021/ja029267j.

[76] D. Musino, C. Rivard, G. Landrot, B. Novales, I. Capron, Tunable Ag Nanoparticle Properties in Cellulose Nanocrystals/ Ag Nanoparticle Hybrid Suspensions by H2O2 Redox Post-Treatment: The Role Of The H2O2/Ag Ratio, Nanomaterials. 10(8) (2020) 1559.

[77] R. Ma, C. Levard, S.M. Marinakos, Y. Cheng, J. Liu, F.M. Michel, G.E. Brown, G. V. Lowry, Size-controlled dissolution of organic-coated silver nanoparticles, Environ. Sci. Technol. 46 (2012) 752–759. https://doi.org/10.1021/es201686j.

List of Figures

Fig. 1. BCN, TBCN, ABCN and HBCN suspensions: visual appearance (top line), STEM images (middle line) and scheme of various surface modifications (bottom line).

Fig. 2. Characterization of unmodified BCNs and BCNs with TEMPO oxidation, aminated or hydrophobic surface modifications: (a) FTIR spectra; (b) XRD patterns.

Fig. 3. Characterizations of BCN-, TBCN-, ABCN-, HBCN-/AgNP hybrid suspensions: (a) UV-Vis spectra; inset: sample pictures; (b) STEM images; (c) XRD patterns.

Fig. 4. (a) UV-Vis spectra and (b) STEM images of TBCN/AgNP hybrid suspension mixed with different volumes of H_2O_2 and, thus, at various α values. (c) Ag_0 content of AgNP_H_2O_2 by XANES fitting, and average AgNP_H_2O_2 diameter determined by STEM as a function of the α parameter in TBCN/AgNP_H_2O_2 hybrids. For Ag_0 value, standard error as considered as the 10% of the measured value.

Fig. 5. (a) Color variation of hybrid suspensions; (b) UV-Vis spectra; (c) STEM images; (d) XRD patterns of BCN-, TBCN-, ABCN-, HBCN-/AgNP_H_2O_2 hybrid suspensions with the addition of 160 µL of H_2O_2 (α = 0.33).

Table 1. Crystalline and surface charge characteristics of native and modified BCNs

Table 2. Summary of characteristics of BCN/AgNP hybrids with and without H_2O_2 redox post-treatment.

Electronic Supplementary Information

Hydroxyl Groups on Cellulose Nanocrystal Surfaces form Nucleation Points for Silver Nanoparticles of Varying Shapes and Sizes

*Dafne Musino,[a] Camille Rivard, [b,c] Gautier Landrot,[b] Bruno Novales,[a] Thierry Rabilloud [d] and Isabelle Capron[a]**

[a] INRAE, BIA, 44316 Nantes, France
[b] SOLEIL Synchrotron, L'Orme des Merisiers, Gif-sur-Yvette, 91192 Saint-Aubin, France
[c] INRAE, TRANSFORM, 44316 Nantes, France
[d] Univ. Grenoble Alpes, CNRS, CEA, IRIG, SYMMES, Laboratoire de Chimie et Biologie des Métaux, 38000 Grenoble, France

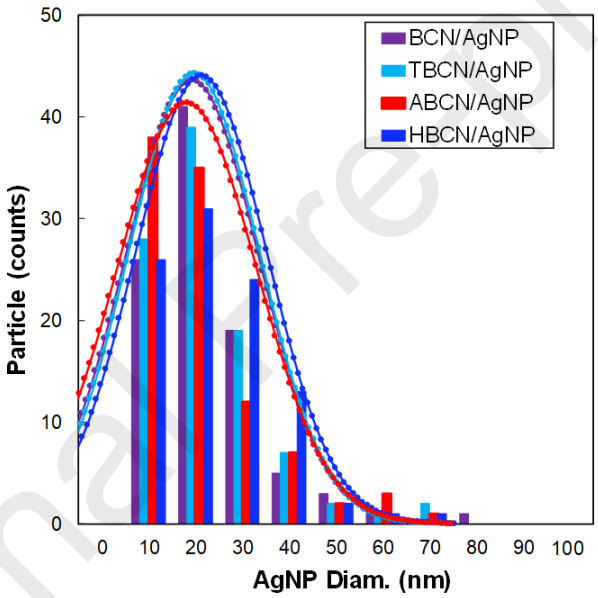

Fig. S1. Size distribution histograms of AgNPs nucleated on BCNs, TBCNs, ABCNs and HBCNs. A total of 100 AgNPs were counted for each sample.

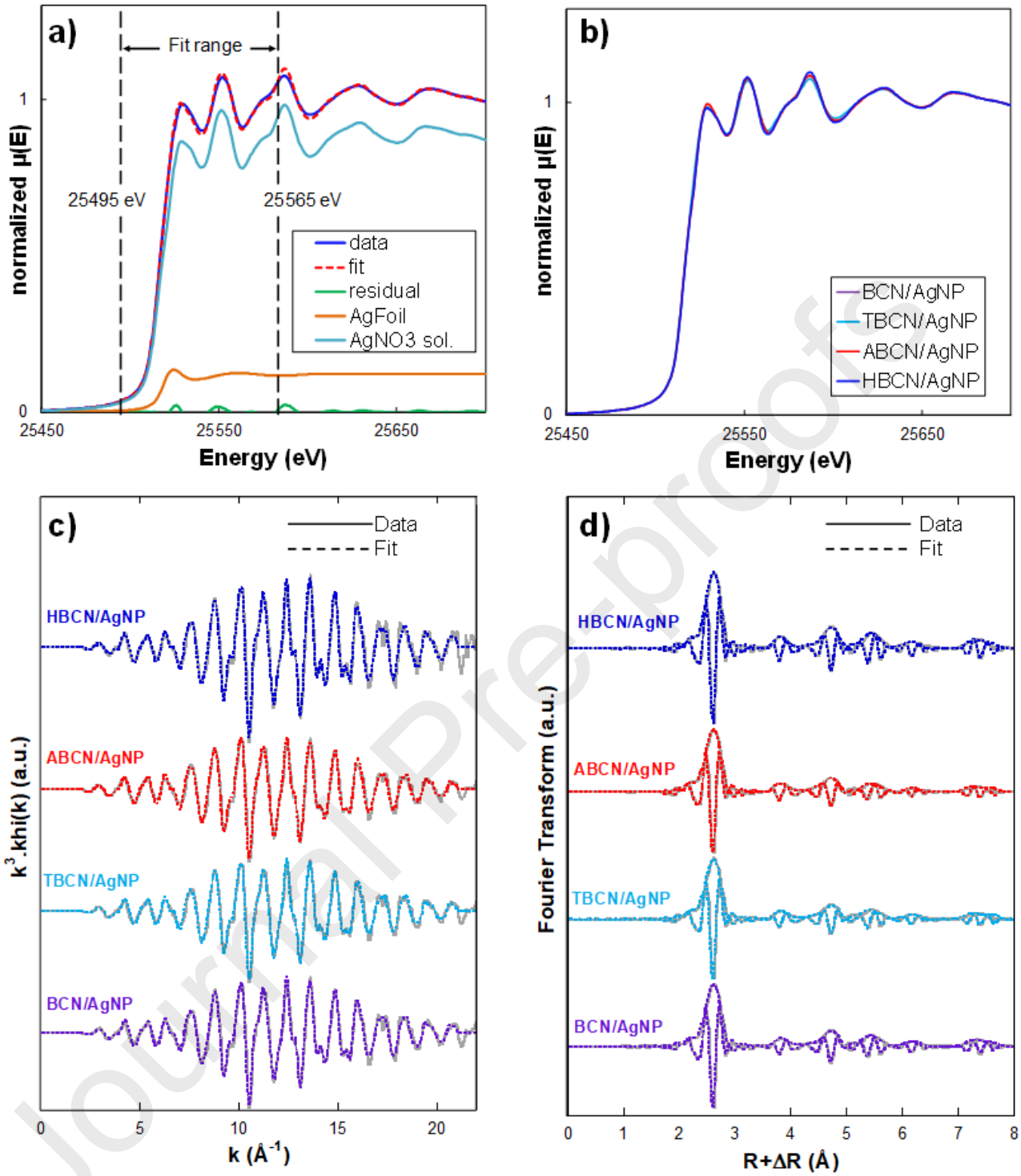

Fig. S2. (a) Example of XANES spectrum fitted by linear combination (LCF) analysis using Agfoil and $AgNO_3$ aqueous solutions as standards; (b) XANES data; (c) EXAFS spectra Fourier transform (solid gray lines) and fit (dotted lines); (d) magnitude and imaginary part (solid gray lines) and fit (dotted lines) of the Fourier transform of BCN-, TBCN-, ABCN- and HBCN/AgNP hybrids.

Table S1. R-factor and Chi-square values for linear combination fitting procedure applied to the XANES region of BCN-, TBCN-, ABCN- and HBCN-/AgNP hybrids.

Hybrid sample	R-factor	Chi-square	Ag_0 (%)[1]
BCN/AgNP	0.0003215	0.01114	90 ± 9
TBCN/AgNP	0.0004912	0.01317	88 ± 9
ABCN/AgNP	0.0003987	0.01086	94 ± 9
HBCN/AgNP	0.0002244	0.00613	97 ± 10

[1] by XANES, the standard error as 10% of the measured value.

Table S2. EXAFS fit results for BCN-, TBCN-, ABCN- and HBCN-/AgNP hybrids.

	Degeneracy of the paths				Debye-Waller factor σ^2				Variation in interatomic distance ΔR (Å)				Interatomic distance R (Å)			
	BCN/ AgNP	**TBCN/ AgNP**	**ABCN/ AgNP**	**HBCN/ AgNP**	**BCN/ AgNP**	**TBCN/ AgNP**	**ABCN/ AgNP**	**HBCN/ AgNP**	**BCN/ AgNP**	**TBCN/ AgNP**	**ABCN /AgNP**	**HBCN/ AgNP**	**BCN/ AgNP**	**TBCN/ AgNP**	**ABCN/ AgNP**	**HBCN/ AgNP**
Ag1 ss	9.5 ± 0.5	9.8 ± 0.5	10.4 ± 0.5	10.9 ± 0.6	0.003	0.003	0.004	0.003	-0.029	-0.029	-0.030	-0.028	2.876	2.877	2.876	2.877
Ag2 ss	2.5 ±1.1	2.6 ± 1.1	3.9 ± 1.5	4.4 ± 1.7	0.003	0.003	0.005	0.004	-0.033	-0.035	-0.037	-0.038	4.076	4.074	4.072	4.071
Ag1 Ag1 at	48*	48*	48*	48*	0.005	0.005	0.005	0.005	-0.044	-0.044	-0.045	-0.042	4.315	4.315	4.314	4.316
Ag3 ss	25.7 ± 3.7	25.0 ± 3.6	25.9 ± 3.6	26.4 ± 3.7	0.006	0.006	0.006	0.005	-0.035	-0.035	-0.036	-0.035	4.997	4.998	4.997	4.997
Ag1 Ag3 ot	96*	96*	96*	96*	0.004	0.005	0.005	0.004	-0.023	-0.023	-0.024	-0.023	5.398	5.399	5.398	5.399
Ag4 ss	6.1 ± 2.3	4.3 ± 3.6	2.7 ± 4.8	5.5 ± 2.5	0.003	0.004	0.005	0.002	-0.010	-0.015	-0.021	-0.012	5.801	5.796	5.790	5.799
Ag1 Ag4 fs	24*	24*	24*	24*	0.006	0.008	0.008	0.006	-0.039	-0.044	-0.051	-0.041	5.772	5.767	5.760	5.770
Ag1 Ag1 fta	12*	12*	12*	12*	0.013	0.014	0.014	0.012	-0.058	-0.058	-0.060	-0.056	5.753	5.753	5.751	5.755
Ag1 Ag4 Ag1 dfs	12*	12*	12*	12*	0.006	0.008	0.008	0.006	-0.039	-0.044	-0.051	-0.041	5.772	5.767	5.760	5.770
Ag5 ss	10.4 ± 6.3	9.8 ± 6.6	8.4 ± 6.2	11.6 ± 6.4	0.004	0.005	0.005	0.004	-0.056	-0.057	-0.057	-0.053	6.439	6.442	6.442	6.442
Ag7 ss	38.8 ± 8.7	38.6 ± 8.8	36.9 ± 7.8	43.2 ± 10.6	0.003	0.004	0.003	0.003	-0.053	-0.054	-0.057	-0.049	7.628	7.630	7.633	7.634
Ag1 Ag7 ot	96*	96*	96*	96*	0.003	0.004	0.004	0.003	-0.028	-0.027	-0.028	-0.027	7.784	7.785	7.786	7.786
Ag3 Ag7 ot	96*	96*	96*	96*	0.004	0.005	0.005	0.004	-0.035	-0.034	-0.035	-0.034	7.777	7.779	7.779	7.779

	BCN/AgNP	**TBCN/AgNP**	**ABCN/AgNP**	**HBCN/AgNP**

R-factor	0.015	0.014	0.012	0.015
ΔE_0	0.89 ± 0.58	0.69 ± 0.54	0.49 ± 0.26	0.47 ± 0.60

ss: single scattering; at: acute triangle; ot: obtuse triangle; fs: forward scattering; dfs: double forward scattering; fta: forward through absorber. Fixed parameters are indicated by a "*". The amplitude reduction factor S_0^2 was fixed at 0.978 Å. Errors obtained for σ^2 were systematically lower than 0.0027; errors obtained for ΔR and R were systematically lower than 0.0150.

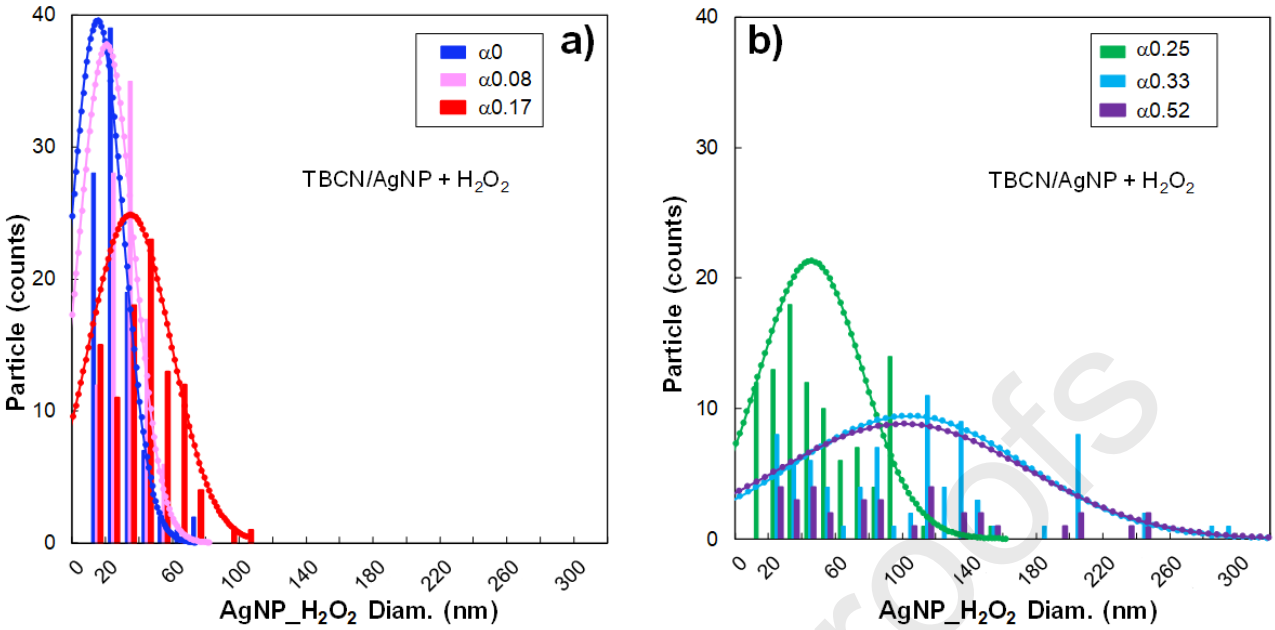

Fig. S3. Size distribution histograms of TBCN/AgNP_H_2O_2 hybrids with various volumes of H_2O_2 added and, consequently, various H_2O_2/AgNP mass ratios. α. from 0 to 0.17 (a), and from 0.25 to 0.52 (b).

Table S3. Average diameter of AgNPs_H_2O_2 in TBCN/AgNP_H_2O_2 hybrid at 7 wt% AgNP treated with different volumes of H_2O_2 (i.e., various H_2O_2 /AgNP mass ratios, α).

H_2O_2/AgNP mass ratio (α)	**Avg AgNP_H_2O_2 diam. (nm)**	**AgNP count**
α0	17.5 ± 12	100
α0.08	21.6 ± 12	100
α0.17	32.5 ± 19	100
α0.25	42.7 ± 28	100
α0.33	97.5 ± 65	80
α0.52	94.1 ± 69	35

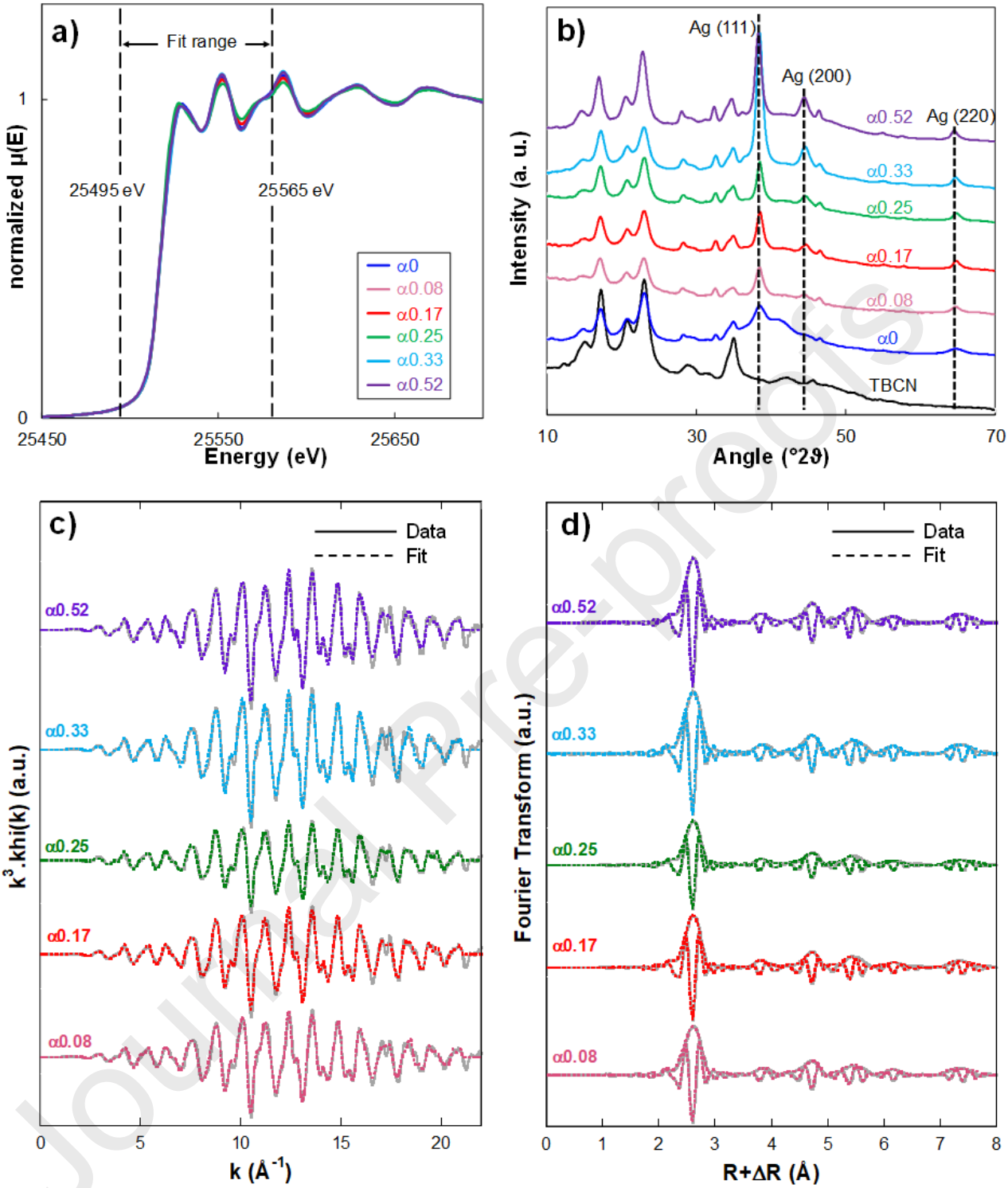

Fig. S4. (a) XANES spectra; (b) XRD diffractograms; (c) EXAFS spectra Fourier transform (solid gray lines) and fit (dotted lines); (d) magnitude and imaginary part (solid gray lines) and fit (dotted lines) of the Fourier transform of TBCN/AgNP_H_2O_2 hybrids at 7 wt% with various volumes of H_2O_2 added (i.e., various H_2O_2/AgNP mass ratios. α).

Table S4. R-factor and Chi-square values for TBCN/AgNP_H_2O_2 hybrids at various H_2O_2/AgNP mass ratios.

H_2O_2/AgNP mass ratio (α)	R-factor	Chi - square	Ag_0 (%)
α0	0.0004912	0.01317	88 ± 9
α0.08	0.0006215	0.01679	79 ± 8
α0.17	0.0005848	0.01588	79 ± 8
α0.25	0.0005803	0.01580	69 ± 7
α0.33	0.0003492	0.00947	91 ± 9
α0.52	0.0005803	0.01236	87 ± 9

[1] by XANES, the standard error as 10% of the measured value.

Table S5. EXAFS fit results for TBCN/AgNP_H_2O_2 hybrid suspensions at various H_2O_2/AgNP ratios, α.

	Degeneracy of the paths						Debye-Waller factor σ²						Variation in interatomic distance ΔR (Å)						Interatomic distance R (Å)					
	α0	**α 0.08**	**α 0.17**	**α 0.25**	**α 0.33**	**α 0.52**	**α0**	**α 0.08**	**α 0.17**	**α 0.25**	**α 0.33**	**α 0.52**	**α0**	**α 0.08**	**α 0.17**	**α 0.25**	**α 0.33**	**α 0.52**	**α0**	**α 0.08**	**α 0.17**	**α 0.25**	**α 0.33**	**α 0.52**
Ag1 ss	9.9 ± 0.5	8.4 ± 0.5	8.5 ± 0.5	7.3 ± 0.4	10.4 ± 0.5	10.0 ± 0.6	0.004	0.003	0.003	0.003	0.003	0.003	-0.029	-0.028	-0.029	-0.029	-0.027	-0.028	2.876	2.877	2.876	2.876	2.878	2.877
Ag2 ss	2.3 ± 1.0	2.3 ± 1.1	2.4 ± 1.2	1.8± 0.9	3.4 ± 1.4	3.4 ± 1.7	0.003	0.003	0.003	0.003	0.003	0.003	-0.037	-0.032	-0.032	-0.031	-0.034	-0.035	4.072	4.077	4.077	4.078	4.075	4.074
Ag1 Ag1 at	48*	48*	48*	48*	48*	48*	0.005	0.005	0.005	0.005	0.005	0.004	-0.044	-0.042	-0.044	-0.044	-0.041	-0.042	4.314	4.316	4.315	4.314	4.317	4.316
Ag3 ss	25.9 ± 3.5	23.7 ± 3.5	23.3 ± 3.5	21.9 ± 3.2	26.3 ± 3.6	26.1 ± 4.0	0.006	0.005	0.005	0.005	0.005	0.005	-0.035	-0.034	-0.035	-0.035	-0.034	-0.035	4.998	4.998	4.997	4.998	4.999	4.997
Ag1 Ag3 ot	96*	96*	96*	96*	96*	96*	0.005	0.004	0.004	0.004	0.004	0.004	-0.023	-0.023	-0.023	-0.023	-0.022	-0.023	5.398	5.399	5.398	5.398	5.400	5.399
Ag4 ss	4.3 ± 3.6	7.0 ± 2.4	12.8 ± 1.5	15.2 ± 1.5	7.1 ± 1.8	7.1 ± 2.2	0.004	0.003	0.002	0.003	0.002	0.002	-0.016	-0.007	0.019	0.029	-0.004	-0.005	5.795	5.804	5.830	5.840	5.807	5.806
Ag1 Ag4 fs	24*	24*	24*	24*	24*	24*	0.008	0.006	0.005	0.006	0.005	0.005	-0.045	-0.035	-0.010	-0.001	-0.031	-0.034	5.766	5.776	5.801	5.810	5.780	5.777
Ag1 Ag1 fta	12*	12*	12*	12*	12*	12*	0.014	0.012	0.012	0.013	0.012	0.012	-0.059	-0.056	-0.058	-0.059	-0.055	-0.056	5.752	5.755	5.753	5.752	5.756	5.755
Ag1 Ag4 Ag1 dfs	12*	12*	12*	12*	12*	12*	0.008	0.006	0.005	0.006	0.005	0.005	-0.045	-0.035	-0.010	-0.001	-0.031	-0.034	5.766	5.776	5.801	5.810	5.780	5.777

Ag5 ss	4.7 ± 3.1	11.0 ± 6.6	9.0 ± 5.1	8.0 ± 4.8	12.8 ± 6.6	13.4 ± 7.9	0.002	0.004	0.003	0.004	0.004	0.004	-0.057	-0.053	-0.052	-0.053	-0.055	-0.056	6.440	6.444	6.444	6.444	6.442	6.441
Ag7 ss	34.7 ± 7.8	37.9 ± 8.2	37.6 ± 8.4	37.7 ± 7.9	38.9 ± 8.9	42.2 ± 11.2	0.003	0.003	0.003	0.003	0.003	0.003	-0.056	-0.052	-0.053	-0.054	-0.048	-0.049	7.631	7.635	7.635	7.633	7.639	7.639
Ag1 Ag7 ot	96*	96*	96*	96*	96*	96*	0.003	0.003	0.003	0.003	0.003	0.003	-0.028	-0.027	-0.027	-0.028	-0.026	-0.026	7.785	7.786	7.785	7.785	7.787	7.786
Ag3 Ag7 ot	96*	96*	96*	96*	96*	96*	0.005	0.004	0.004	0.004	0.004	0.004	-0.034	-0.033	-0.034	-0.034	-0.033	-0.034	7.778	7.779	7.778	7.779	7.780	7.779

	α0	**α 0.08**	**α 0.17**	**α 0.25**	**α 0.33**	**α 0.52**
R-factor	0.011	0.018	0.019	0.020	0.015	0.019
ΔE_0	0.59 ± 0.53	0.72 ± 0.65	0.59 ± 0.67	0.45 ± 0.65	0.51 ± 0.60	0.451 ± 0.70

ss: single scattering; at: acute triangle; ot: obtuse triangle; fs: forward scattering; dfs: double forward scattering; fta: forward through absorber. Fixed parameters are indicated by a "*". The amplitude reduction factor S_0^2 was fixed at 0.978 Å. Errors obtained for σ^2 were systematically lower than 0.0018; errors obtained for ΔR and R were systematically lower than 0.0096.

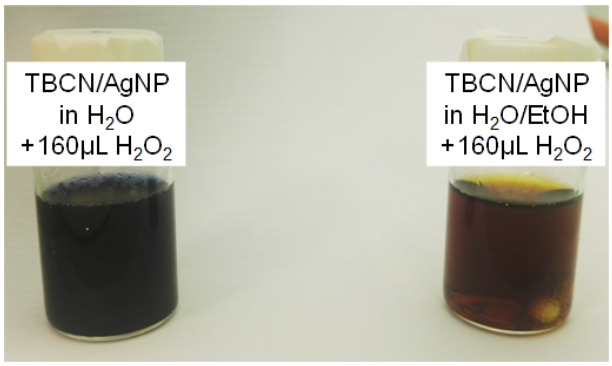

Fig. S5. Comparison between TBCN/AgNP prepared with the addition of 160 µL of H_2O_2 (α = 0.33) in a pure water medium or in a H_2O/EtOH mixture. The presence of ethanol seems to affect the H_2O_2 post-treatment since the color suspension did not turn blue like the pure water suspension.

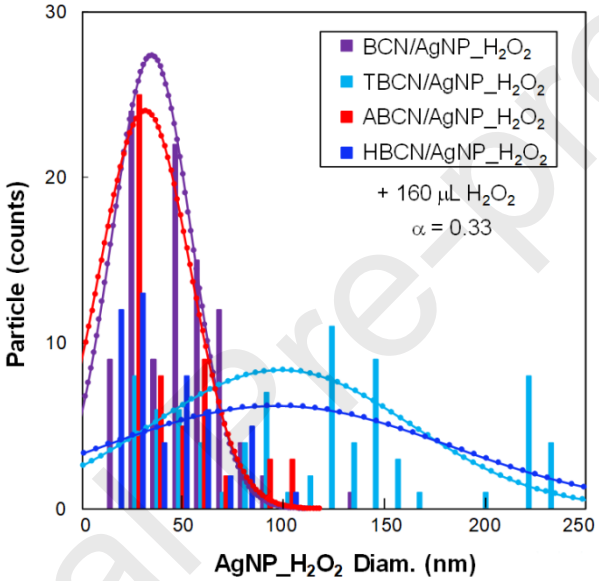

Fig. S6. Size distribution histograms of AgNPs_H_2O_2 in BCN-. TBCN-. ABCN. HBCN/AgNP_H_2O_2 hybrids at H_2O_2 /AgNP ratios. α, equal to 0.33.

Table S6. Average diameter of AgNPs_H_2O_2 in BCN-. TBCN-. ABCN. HBCN/AgNP_H_2O_2 hybrids at H_2O_2 /AgNP mass ratios. α, equal to 0.33.

Hybrid sample + 160 µL H_2O_2 (α= 0.33)	Avg AgNP_H_2O_2 diam. (nm)	AgNP count
BCN/AgNP_H_2O_2	32.5 ± 19	100
TBCN/AgNP_H_2O_2	97.5 ± 65	80
ABCN/AgNP_H_2O_2	95.4 ± 87	100
HBCN/AgNP_H_2O_2	29.4 ± 22	100

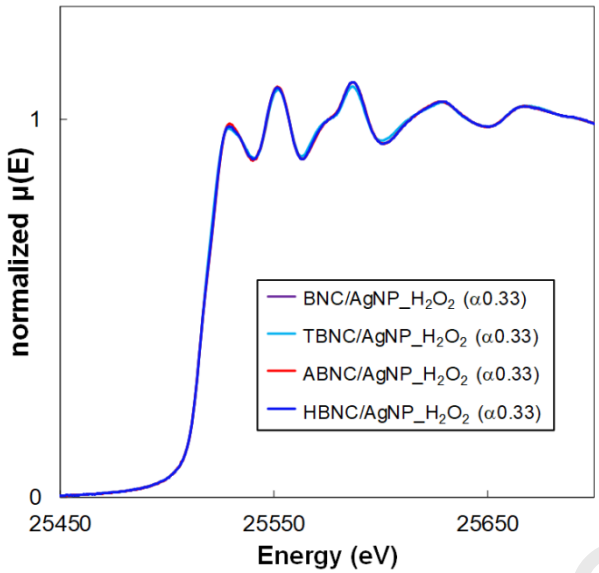

Fig. S7. XANES spectra of BCN-., TBCN-., ABCN-. and HBCN/ AgNP_H_2O_2 hybrids mixed with 160 μL of H_2O_2 (α = 0.33).

Table S7. R-factor and Chi-square values for BCN-. TBCN-. ABCN- and HBCN-/ AgNP_H_2O_2 hybrid suspensions mixed with 160 μL of H_2O_2 (α = 0.33).

Hybrid sample + 160 μL H_2O_2 (α= 0.33)	**R-factor**	**Chi-square**	**Ag_0 (%)**
BCN/AgNP_H_2O_2	0.0002663	0.00783	93 ± 9
TBCN/AgNP_H_2O_2	0.0003492	0.00947	91 ± 9
ABCN/AgNP_H_2O_2	0.0001964	0.00538	97 ± 10
HBCN/AgNP_H_2O_2	0.000187	0.00509	97 ± 10

[1] by XANES, the standard error as 10% of the measured value.

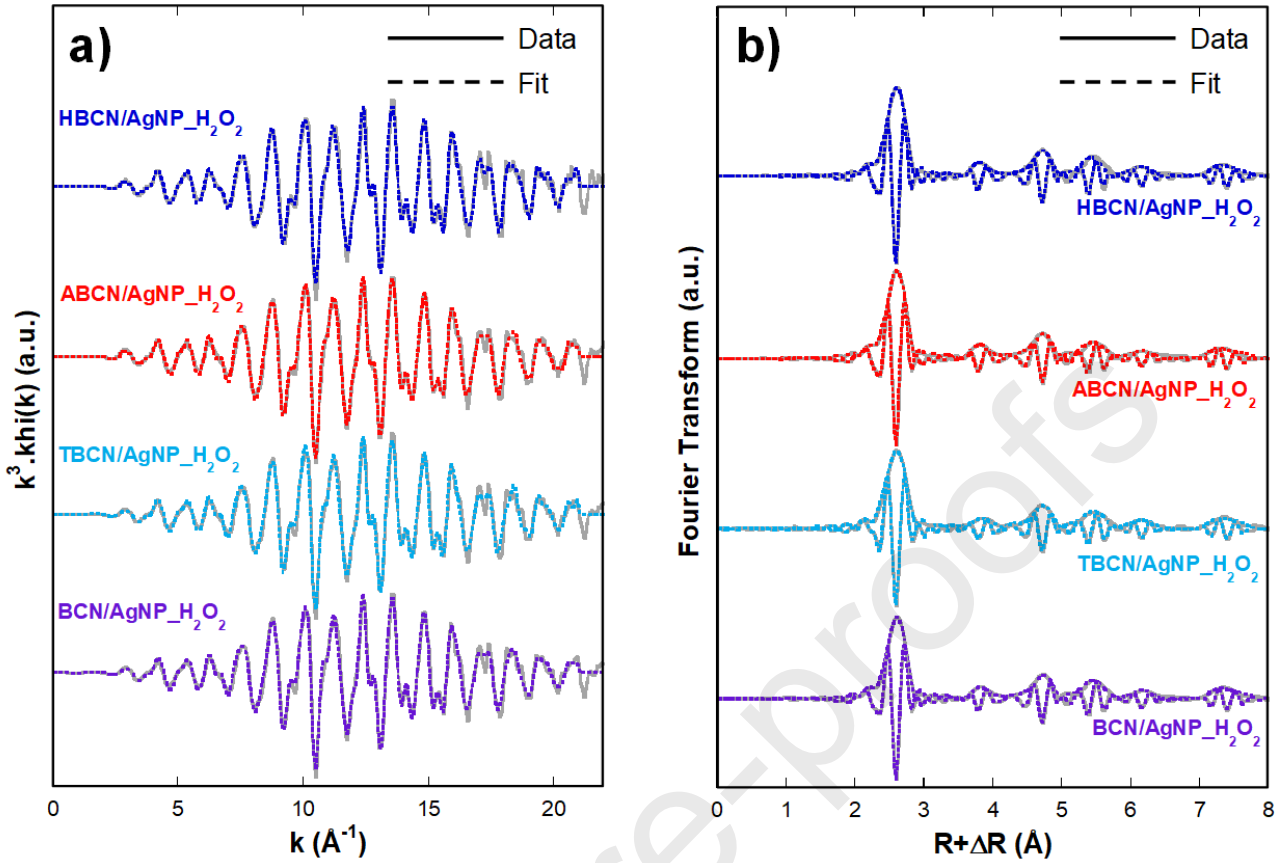

Fig. S8. (a) EXAFS spectra Fourier transform (solid gray lines) and fit (dotted lines); (d) magnitude and imaginary part (solid gray lines) and fit (dotted lines) of the Fourier transform of BCN-., TBCN-., ABCN-. and HBCN/ AgNP_H_2O_2 hybrids with 160µL of H_2O_2 (α= 0.33).

Table S8. EXAFS fit results for BCN-. TBCN-. ABCN- and HBCN-/ AgNP_H_2O_2 hybrid suspensions with 160 µL of H_2O_2 (α = 0.33).

	Degeneracy of the paths				Debye-Waller factor σ²				Variation in interatomic distance ΔR (Å)				Interatomic distance R (Å)			
	BCN	**TBCN**	**ABCN**	**HBCN**	**BCN**	**TBCN**	**ABCN**	**HBCN**	**BCN**	**TBCN**	**ABCN**	**HBCN**	**BCN**	**TBCN**	**ABCN**	**HBCN**
Ag1 ss	10.2 ± 0.6	10.4 ± 0.5	11.5 ± 0.6	11.0 ± 0.6	0.0030	0.0030	0.0031	0.0030	-0.027	-0.027	-0.028	-0.030	2.879	2.878	2.878	2.876
Ag2 ss	3.3 ±1.5	3.4 ± 1.4	4.7 ± 1.8	4.7 ± 1.8	0.0032	0.0032	0.0038	0.0038	-0.032	-0.034	-0.035	-0.038	4.077	4.075	4.074	4.071
Ag1 Ag1 at	48*	48*	48*	48*	0.0045	0.0045	0.0047	0.0044	-0.040	-0.041	-0.041	-0.045	4.318	4.317	4.317	4.313
Ag3 ss	27.1 ± 3.9	26.3 ± 3.6	27.9 ± 4.0	26.5 ± 3.7	0.0049	0.0048	0.0049	0.0046	-0.034	-0.034	-0.034	-0.038	4.999	4.999	4.998	4.995
Ag1 Ag3 ot	96*	96*	96*	96*	0.0040	0.0039	0.0040	0.0038	-0.022	-0.022	-0.022	-0.024	5.400	5.400	5.399	5.397
Ag4 ss	5.6 ± 2.5	7.1 ± 1.8	2.8 ± 4.6	12.9 ± 1.4	0.0023	0.0019	0.0032	0.0015	-0.009	-0.004	-0.017	0.016	5.802	5.807	5.794	5.827
Ag1 Ag4 fs	24*	24*	24*	24*	0.0053	0.0049	0.0063	0.0044	-0.036	-0.031	-0.044	-0.014	5.775	5.780	5.767	5.797
Ag1 Ag1 fta	12*	12*	12*	12*	0.0120	0.0120	0.0125	0.0118	-0.054	-0.055	-0.055	-0.060	5.757	5.756	5.756	5.751
Ag1 Ag4 Ag1 dfs	12*	12*	12*	12*	0.0053	0.0049	0.0063	0.0044	-0.036	-0.031	-0.044	-0.014	5.775	5.780	5.767	5.797
Ag5 ss	13.0 ± 6.9	12.8 ± 6.6	12.3 ± 7.6	10.7 ± 5.4	0.0038	0.0038	0.0041	0.0029	-0.052	-0.055	-0.057	-0.060	6.445	6.442	6.440	6.437
Ag7 ss	38.0 ± 8.7	38.9 ± 8.9	34.9 ± 7.5	44.7 ± 10.7	0.0025	0.0027	0.0022	0.0029	-0.048	-0.048	-0.051	-0.052	7.639	7.639	7.636	7.635
Ag1 Ag7 ot	96*	96*	96*	96*	0.0028	0.0028	0.0027	0.0029	-0.025	-0.026	-0.026	-0.028	7.787	7.787	7.787	7.784
Ag3 Ag7 ot	96*	96*	96*	96*	0.0037	0.0037	0.0036	0.0037	-0.033	-0.033	-0.034	-0.036	7.780	7.780	7.779	7.776

	BCN	**TBCN**	**ABCN**	**HBCN**
R-factor	0.016	0.015	0.015	0.015
ΔE_0	0.99 ± 0.62	0.52 ± 0.60	0.49 ± 0.60	0.21 ± 0.60

ss: single scattering; at: acute triangle; ot: obtuse triangle; fs: forward scattering. dfs: double forward scattering; fta: forward through absorber. Fixed parameters are indicated by a "*". The amplitude reduction factor S_0^2 was fixed at 0.978 Å. Errors obtained for σ^2 were systematically lower than 0.0018; errors obtained for ΔR and R were systematically lower than 0.0097.